The Astrophysical Journal Letters, 918:L25 (20pp), 2021 September 10 https://doi.org/10.3847/2041-8213/ac1e2d

On the Detection of Exomoons Transiting Isolated Planetary-mass Objects

Mary Anne Limbach[1], Johanna M. Vos[2], Joshua N. Winn[3], René Heller[4,5], Jeffrey C. Mason[6], Adam C. Schneider[7,8], and Fei Dai[9]
[1] Department of Physics and Astronomy, Texas A&M University, 4242 TAMU, College Station, TX 77843-4242 USA; maryannelimbach@gmail.com
[2] Department of Astrophysics, American Museum of Natural History, Central Park West at 79th Street, New York, NY 10024, USA
[3] Department of Astrophysical Sciences, Peyton Hall, 4 Ivy Lane, Princeton, NJ 08544, USA
[4] Max Planck Institute for Solar System Research, Justus-von-Liebig-Weg 3, 37077 Göttingen, Germany
[5] Georg-August-Universität Göttingen, Institut für Astrophysik, Friedrich-Hund-Platz 1, 37077 Göttingen, Germany
[6] Department of Physics, New Mexico Institute of Mining and Technology, 801 Leroy Place, Socorro, NM 87801, USA
[7] United States Naval Observatory, Flagstaff Station, 10391 West Naval Observatory Road, Flagstaff, AZ 86005, USA
[8] Department of Physics and Astronomy, George Mason University, MS3F3, 4400 University Drive, Fairfax, VA 22030, USA
[9] Division of Geological and Planetary Sciences, California Institute of Technology, 1200 East California Boulevard, Pasadena, CA 91125, USA
Received 2021 June 8; revised 2021 August 9; accepted 2021 August 17; published 2021 September 7

Abstract

All-sky imaging surveys have identified several dozen isolated planetary-mass objects (IPMOs) far away from any star. Here we examine the prospects for detecting transiting moons around these objects. We expect transiting moons to be common, occurring around 10%–15% of IPMOs, given that close-orbiting moons have a high geometric transit probability and are expected to be a common outcome of giant planet formation. The IPMOs offer an advantage over other directly imaged planets in that high-contrast imaging is not necessary to detect the photometric transit signal. For at least 30 (>50%) of the currently known IPMOs, observations of a single transit with the James Webb Space Telescope would have low enough forecast noise levels to allow for the detection of an Io- or Titan-like moon. The intrinsic variability of the IPMOs will be an obstacle. Using archival time-series photometry of IPMOs with the Spitzer Space Telescope as a proof of concept, we found evidence for a fading event of 2MASS J1119–1137 AB that might have been caused by intrinsic variability but is also consistent with a single transit of a habitable-zone 1.7 $R_\oplus$ exomoon. Although the interpretation of this particular event is inconclusive, the characteristics of the data and the candidate signal suggest that Earth-sized habitable-zone exomoons around IPMOs are detectable with existing instrumentation.

Unified Astronomy Thesaurus concepts: Natural satellites (Extrasolar) (483); Free floating planets (549); Transits (1711); Exoplanets (498); Habitable zone (696)

1. Introduction

Many methods have been suggested to search for the moons of planets outside the solar system, which are often called "exomoons." As reviewed by Heller (2018), about a dozen signals possibly attributable to exomoons have been described in the literature based on gravitational microlensing (Bennett et al. 2014; Miyazaki et al. 2018), signatures in transit spectra (Oza et al. 2019; Gebek & Oza 2020), gaps in circumplanetary rings (Kenworthy & Mamajek 2015), transit-timing variations (TTVs) accompanied by exomoon transits of the host star (Rodenbeck et al. 2018; Teachey et al. 2018, 2020; Teachey & Kipping 2018; Kreidberg et al. 2019), TTVs (Fox & Wiegert 2020; Kipping 2020), direct imaging (Lazzoni et al. 2020), and absorption by gas possibly associated with an orbiting moon (Ben-Jaffel & Ballester 2014). Follow-up, confirmation, and further characterization of these exomoon candidates have proven difficult, making it important to devise more methods for detecting exomoons.

Isolated planetary-mass objects (IPMOs) offer another opportunity for exomoon detection. The IPMOs are objects that have the low luminosities and spectral characteristics expected of giant planets but can be observed in detail in the absence of a bright host star. They have also been called free-floating planets, starless planets, or rogue planets. They are to be distinguished from the dozen directly imaged planets that have been detected via high-contrast imaging in the vicinity of bright host stars (e.g., Bowler 2016).

Several dozen IPMO candidates have been identified in the literature through their spectral and kinematic signatures of youth and/or low gravity (see Table 1 and references therein). Depending on their spectral characteristics, IPMOs have been classified as Y, T, or L dwarfs. They are objects for which evolutionary models indicate that the mass is less than 13 $M_{\rm Jup}$, making them qualify as planets according to the deuterium-burning criterion (Spiegel et al. 2011). Many of the known IPMOs are young, bright, and well characterized (e.g., Faherty et al. 2013; Liu et al. 2013; Schneider et al. 2014, 2016; Gagné et al. 2015, 2017). Some colder IPMOs with unknown ages have been detected, despite their lower luminosities, by virtue of their proximity to the Sun. For example, WISE 0855–0714 has an estimated mass of 1.5–8 $M_{\rm Jup}$ and is located 2 pc from the Sun, giving it an apparent magnitude of 14.0 in the 4.6 μm WISE W2 band (Luhman 2014). There are other Y, T, and L dwarfs that may be IPMOs but for which estimated masses are not available in the literature. The IPMOs are most similar to the directly imaged exoplanet population in composition, mass, and age. Directly imaged exoplanets span the same spectral range as IPMOs from Y dwarfs (WD 0806–661b; Luhman et al. 2011) to early L dwarfs (β Pic b; Lagrange et al. 2009, 2010). Indeed, some of the objects included in Table 1, a list of IPMOs, are companions that are sufficiently separated from their host to allow for variability studies without the use of high-contrast imaging, such as the exoplanets Ross 458(AB)c (Goldman et al. 2010; Scholz 2010) and COCONUTS-2b (Zhang et al. 2021).

Table 1
IPMOs and Candidate IPMOs

Object	SpT	K (mag)	W2[a] (mag)	Mass[b] ($M_{\rm Jup}$)	Assoc. Member?	JNSPP (ppm)	5σ Limit[c] ($R_{\rm Titan}$)	5σ Limit[c] ($R_{\oplus}$)	Refs.
2MASS 02103857–3015313	L0	13.50	12.65	13.0 ± 4.3	Tuc-Hor	49	0.56	0.23	10
2MASS J0249–0557c[d]	L2	14.78	13.59	11.6 ± 1.3	β Pic	63	0.64	0.26	16
2MASS 01531463–6744181	L2	14.42	13.22	11.89 ± 5.36	Tuc-Hor cand.	53	0.59	0.24	10
2MASS J2208136+292121	L3	14.12	12.91	12.6 ± 0.6	β Pic	45	0.54	0.22	16
2MASS 03421621–6817321	L4	14.54	13.48	12.4 ± 6.1	AB Dor cand.	60	0.62	0.25	10
2M1207b[d]	L6	16.93	...	8±2	TW Hya	165	1.04	0.42	18, 19
2MASS 22443167+2043433	L6.5	14.02	12.11	10.5 ± 1.5	AB Dor	56	0.60	0.24	10, 23, 25
WISEA J114724.10–204021.3	L7	14.87	13.09	5–13	TW Hya cand.	74	0.69	0.28	3, 4, 10
2MASS J11193254–1137466 AB	L7	14.75	12.88	4–8[e]	TW Hya cand.	66	0.66	0.26	4, 5, 10
WISE J174102.78–464225.5	L7	13.44	11.67	4–21	AB Dor cand.	45	0.54	0.22	7
PSO J318.5338–22.8603	L7	14.44	12.46	9–15	β Pic	54	0.59	0.24	8, 10
2MASS 00470038+6803543	L7	13.05	11.27	11.8 ± 2.6	AB Dor	54	0.59	0.24	10, 23
HD 203030b[d]	L7.5	16.16	...	11 ± 4	Field	91	0.59	0.24	20
2MASS J13243553+6358281	T2	14.06	12.29	11–12	AB Dor	64	0.65	0.26	14, 23
SIMP J013656.5+093347	T2	12.6	10.96	11.7–13.7	Car-N cand.	40	0.51	0.20	9, 23
ULAS J004757.41+154641.4	T2	16.42	14.86	8.3 ± 0.9	Argus cand.	204	1.15	0.47	17
PSO J168.1800–27.2264	T2.5	16.65	14.98	8.0 ± 0.7	Argus cand.	218	1.19	0.48	17
SDSS J152103.24+013142.7	T3	15.57	13.94	8.5 ± 0.9	Argus cand.	127	0.91	0.37	17
2MASS J00132229–1143006	T4	15.76	14.32	8.1 ± 0.7	Argus cand.	154	1.00	0.40	17
WISEPA J081958.05–033529.0	T4	14.64	13.08	5.7 ± 0.5	β Pic cand.	83	0.73	0.30	17
SDSS J020742.48+000056.2	T4.5	16.72	15.05	7.9 ± 0.8	Argus cand.	226	1.21	0.49	17
WISE J223617.59+510551.9	T5	14.57	12.50	12.1 ± 1.3	Car-N cand.	79	0.71	0.29	17
SDSS J111010.01+011613.1	T5.5	16.05	13.92	10–12	AB Dor	158	1.01	0.41	6, 23
ULAS J154701.84+005320.3	T5.5	18.21	15.89	5.9 ± 0.9	Argus cand.	470	1.75	0.71	17
ULAS J120744.65+133902.7	T6	18.67	15.88	4.9 ± 0.8	Argus cand.	467	1.74	0.70	17
ULAS J081918.58+210310.4	T6	17.18	15.24	11.2 ± 1.2	AB Dor cand.	320	1.44	0.58	17
WISEPA J062720.07–111428.8	T6	15.51	13.25	11.1 ± 0.9	AB Dor cand.	113	0.86	0.35	17
CFBDS J232304.41–015232.3	T6	17.23	15.07	4.8 ± 0.7	β Pic cand.	290	1.37	0.55	17
SDSSp J162414.37+002915.6	T6	15.61	13.09	11.0 ± 0.8	Car-N cand.	105	0.83	0.33	17
ULAS J075829.83+222526.7	T6.5	17.87	15.08	4.8 ± 0.8	Argus cand.	292	1.38	0.56	17
WISE J024124.73–365328.0	T7	···	14.35	5.1 ± 0.4	Argus cand.	197	1.13	0.46	17
2MASSI J1553022+153236	T7	15.94	13.03	12.0 ± 1.3	Car-N cand.	102	0.81	0.33	17
WISE J031624.35+430709.1	T8	···	14.64	4.8 ± 0.7	Car-N cand.	230	1.22	0.49	17
WISEPC J225540.74–311841.8	T8	17.42	14.16	2.3 ± 0.2	β Pic cand.	179	1.08	0.44	17
Ross 458(AB)c[d]	T8	16.96	13.77	6.8–15.9	Field	147	0.75	0.30	1, 2
ULAS J130217.21+130851.2	T8.5	18.28	14.87	5.6 ± 0.9	Car-N cand.	260	1.30	0.53	17
WISE J233226.49–432510.6	T9	···	14.96	3.8 ± 0.7	AB Dor cand.	273	1.33	0.54	17
UGPS J072227.51–054031.2	T9	17.07	12.21	6–9	Field	69	0.52	0.21	11
COCONUTS-2b[d]	T9	20.03	14.53	4.4–7.8	Field	217	1.19	0.48	26, 27
WISEA J205628.88+145953.6	Y0	20.01	13.84	8–20	Field	175	0.82	0.33	24
WISEA J220905.75+271143.6	Y0	···	14.77	8–19	Field	284	1.05	0.42	24
WISE J222055.31–362817.4	Y0	21.33	14.71	8–20	Field	275	1.03	0.42	24
WISEA J163940.84–684739.4	Y0	···	13.54	5–14	Field	151	0.76	0.31	12, 15, 24
WISEA J173835.52+273258.8	Y0	20.58	14.50	5–14	Field	246	0.97	0.39	24
WISE J035934.06–540154.6	Y0	22.8	15.38	8–20	Field	397	1.24	0.50	12, 24
WISEA J041022.75+150247.9	Y0	19.91	14.11	8–20	Field	201	0.88	0.36	11, 24
WISEA J114156.67–332635.5	Y0	···	14.61	3–8	Field	261	1.00	0.40	24
WISEA J120604.25+840110.5	Y0	···	15.06	6–14	Field	332	1.13	0.46	24
WISEA J082507.37+280548.2	Y0.5	···	14.58	3–8	Field	256	0.99	0.40	24
WISEA J035000.31–565830.5	Y1	···	14.75	3–8	Field	281	1.04	0.42	12, 24
WISE J064723.23–623235.5	Y1	···	15.22	5–13	Field	363	1.18	0.48	24
WD 0806–661b[d]	Y1	···	16.88	7–9	Field	1023	1.98	0.80	21, 24
WISE J154151.65–225024.9	Y1	21.70	14.25	8–20	Field	216	0.91	0.37	11, 24
WISE J053516.80–750024.9	$\geqslant$ Y1	···	14.90	8–20	Field	304	1.08	0.44	24
WISEA J083011.95+283716.0	$\geqslant$ Y1	···	16.05	4–13	Field	591	1.51	0.61	28
WISE J085510.83–071442.5	>Y2	···	14.02	1.5–8	Field	192	0.86	0.35	13, 24
WISEPA J182831.08+265037.8	>Y2	23.48	14.35	3–8	Field	228	0.94	0.38	24

Notes.
[a] WISE band magnitudes. In some cases, Spitzer [4.5]- or M-band magnitudes are substituted for W2.
[b] These are model-dependent masses, which are dependent on the assumed age. For young IPMOs, age is based on association with a moving group (i.e., with proper motions, radial velocity, and parallax). Some of these IPMOs are candidates for moving groups (rather than bona fide members). The quoted masses are likely to change as moving group ages are revised in the literature.
[c] The "limit" is the estimated 5σ minimum detectable moon radius for each IPMO based on the JNSPP.
[d] Companions that are sufficiently separated from their host to allow for variability monitoring.
[e] Total mass of the binary planet system assuming association with TW Hya; magnitudes are for the unresolved binary.

References. (1) Burningham et al. (2011), (2) Manjavacas et al. (2019b), (3) Schneider et al. (2016), (4) Schneider et al. (2018), (5) Best et al. (2017a), (6) Gagné et al. (2015), (7) Schneider et al. (2014), (8) Liu et al. (2013), (9) Gagné et al. (2017), (10) Faherty et al. (2016), (11) Cushing et al. (2011), (12) Dupuy & Kraus (2013), (13) Luhman (2014), (14) Gagné et al. (2018), (15) Schneider et al. (2015), (16) Dupuy et al. (2018), (17) Zhang et al. (2021), (18) Zhou et al. (2016), (19) Mohanty et al. (2007), (20) Metchev & Hillenbrand (2006), (21) Luhman et al. (2012), (22) Best et al. (2020), (23) Kirkpatrick et al. (2021), (24) Leggett et al. (2017), (25) Vos et al. (2018), (26) Kirkpatrick et al. (2011), (27) Zhang et al. (2021), (28) Bardalez Gagliuffi et al. (2020).

In this paper, we consider the possibility that IPMOs have moons similar to the major moons of Jupiter and Saturn. The moons of IPMOs might form in one of two ways. If the IPMO was formerly part of an ordinary planetary system centered on a star, its moons could have formed in a circumplanetary disk within the larger circumstellar disk, as is thought to have happened for Jupiter and Saturn (Canup & Ward 2002; Mosqueira & Estrada 2003; Sasaki et al. 2010). Then, when the planet was ejected into interstellar space by dynamical interactions, the moons would have had a reasonable probability of remaining bound to the planet. According to calculations by Rabago & Steffen (2018) and Hong et al. (2018), Io-like moons would have a 55% (Hong et al. 2018) to 85% (Rabago & Steffen 2018) chance of surviving intact. Alternatively, the IPMO might have formed in isolation as an unusually low-mass outcome of star formation processes. In that case, there would be debate over whether to call a small companion of an IPMO a "moon," a "planet," or something else. For simplicity, we will refer to the secondary body as a moon in either case, following a precedent established in the literature (Bennett et al. 2014; Skowron et al. 2014; Miyazaki et al. 2018; Avila et al. 2021; Tamburo et al. 2021).

In this paper, we will show that young IPMOs are attractive targets for exomoon searches. In the first place, IPMOs (unlike ordinary planets) can be observed without the problems associated with the overwhelming glare of a nearby host star, greatly simplifying exomoon detection and further characterization. Second, the currently known examples of young IPMOs are sufficiently bright for high signal-to-noise ratio (S/N) observations with almost any mid- to large-class ground or space-based telescope. Because IPMOs emit mainly at infrared wavelengths, NASA's James Webb Space Telescope (JWST) is well poised to detect and study their exomoons. These two advantages should make it possible to search for exomoons around IPMOs in many of the same ways that astronomers are already searching for exoplanets around nearby stars. This includes looking for exomoons via direct imaging, radial velocity monitoring, astrometric variations, and transits. Earlier authors considered applying these methods to directly imaged exoplanets orbiting stars (Cabrera & Schneider 2007; Agol et al. 2015; Heller 2016; Vanderburg et al. 2018; Lazzoni et al. 2020), but for IPMOs, the observational requirements are more easily met because high-contrast imaging is unnecessary to detect the IPMO. Indeed, the gravitational-lensing technique has already been used to identify a signal (MOA-2011-BLG-262Lb) that could have arisen from an exomoon orbiting an IPMO, although the data do not strongly rule out the possibility that the signal is from a planet orbiting a low-mass star (Bennett et al. 2014).

This paper focuses on transit detection because it seemed possible to us that the method can succeed in the near future. As we will argue, existing or near-future instrumentation is capable of detecting exomoons analogous to the solar system moons in systems where it is reasonable to expect the exomoon occurrence rate to be high. In this sense, our work investigating the prospects for detecting transiting moons around IPMOs is analogous to earlier work on the prospects of finding transiting planets around low-mass stars (Gould et al. 2003; Nutzman & Charbonneau 2008) and brown dwarfs (Triaud et al. 2013; Tamburo & Muirhead 2019).

2. Expected Exomoon Transit Probabilities, Depths, and Frequencies

2.1. Exomoon Transit Probabilities

2.1.1. Transit Probabilities Based on Solar System Moon Statistics

We have few observational constraints on the exomoon population (Hippke 2015; Teachey et al. 2018). However, there is an extensive and growing literature on the formation of moons around gas giants, including N-body simulations of moon formation via accretion in circumplanetary disks (Canup & Ward 2006; Ogihara & Ida 2012; Heller & Pudritz 2015a, 2015b; Miguel & Ida 2016; Cilibrasi et al. 2018, 2021; Moraes et al. 2018; Inderbitzi et al. 2020; Ronnet & Johansen 2020) and direct imaging of moon-forming disks (Benisty et al. 2021). These studies suggest that moon formation around gas giants well separated from a host star is common and that the solar system moons are representative of moon formation around young, accreting giant planets. Simulations show that at least one large moon ($>10^{-6}\,M_{\rm planet}$) forms in $\gtrsim$80% of systems (Cilibrasi et al. 2021). Simulations also predict that these moons form in close-in orbits, $\lesssim$30 planetary radii, resembling the Galilean moons (Ogihara & Ida 2012; Heller & Pudritz 2015a). Therefore, lacking any observations of the actual exomoon population, for this work, we will assume that IPMOs have moons similar to the moons orbiting the gas giant planets in the solar system.

We calculate the geometric transit probabilities for the solar system gas giant moons as viewed by a randomly oriented observer outside our solar system. Assuming circular orbits and that the secondary companion is much smaller than the primary object, the geometric transit probability is R/a, the radius of the primary divided by the orbital radius (Winn 2010). Figure 1 (left panel) shows the transit probabilities for the large moons of the solar system, where "large" is defined as a moon-to-planet mass ratio exceeding 4×10^{-7}, chosen such that the lowest-mass moon that qualifies is Neptune's moon Proteus. The transit probabilities range between about 5% and 25%. The median transit probability of the 16 largest moons is 10%. If we restrict the sample to the closest-orbiting large moon around each gas giant planet, the median transit probability is 20%. Figure 1 (right panel) gives the range of inclination angles for transits to occur. The probability that there is at least one transiting system ($n\geqslant1$) within a sample of N unrelated primary objects with identical radii (R) and secondary objects at identical orbital distances (a) is

$$P_{n\geqslant1}(N) = 1-\left(1-\frac{R}{a}\right)^{N}. \quad (1)$$

Figure 2 (left panel) shows $P_{n\geqslant1}(N)$ for four cases. The black dashed–dotted curve is for planets like Jupiter, orbiting at 5 au around Sun-like stars. The blue dotted line is for planets like Mercury, orbiting at 0.4 au around Sun-like stars. The gray dashed curve refers to Europa's orbit around Jupiter, and the red curve refers to Io's orbit around Jupiter. As an example, in a sample of $N=10$ objects with orbiting secondary companions, the geometric probability that at least one of the secondaries is transiting is 10% for the case of Mercury–Sun analogs, 68% for Europa–Jupiter analogs, and 85% for Io–Jupiter analogs. Figure 2 (right panel) shows the fractional loss of light (transit depth) that would occur during a transit of a

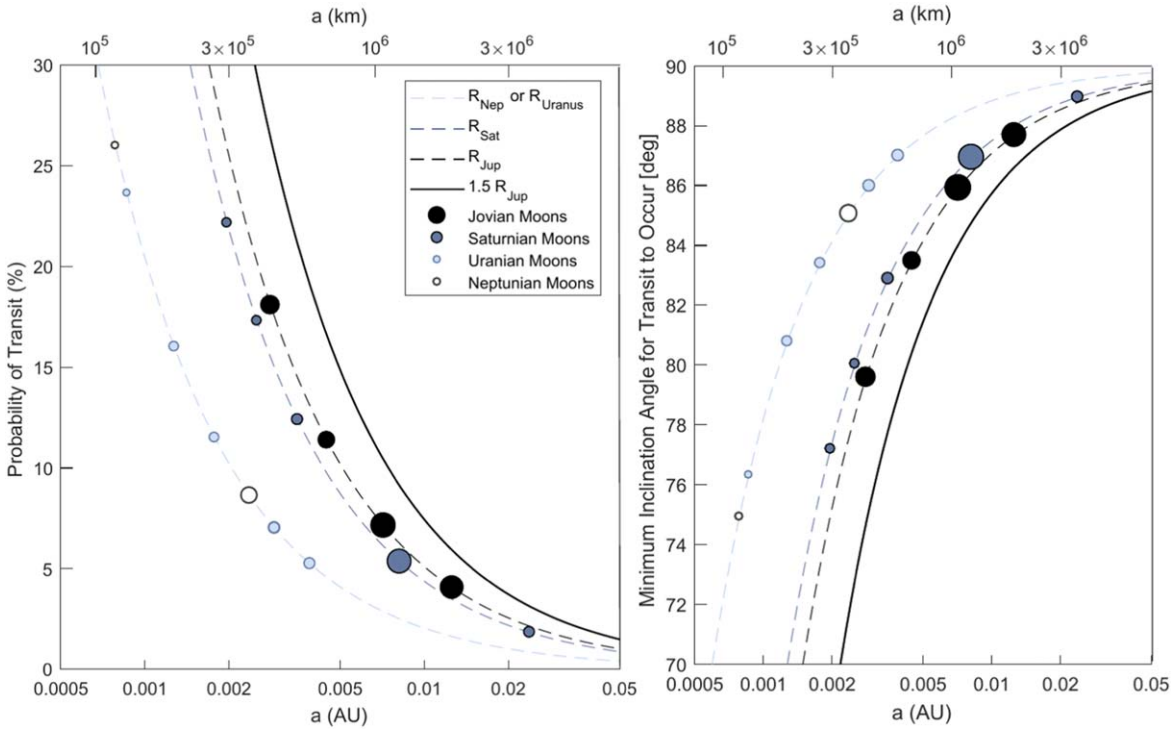

Figure 1. Left: geometric exomoon transit probabilities, assuming a random viewing direction. The curves correspond to planets with radii of (from left to right) Uranus/Neptune, Saturn, Jupiter, and 1.5 times Jupiter. Circles represent the actual solar system moons with masses exceeding 4×10^{-7} of the mass of the host planet. The median transit probability of these moons is 10%. Right: minimum inclination angle for transits vs. orbital radius. The closest-orbiting large moons of the solar system would transit over an unusually wide range of inclinations.

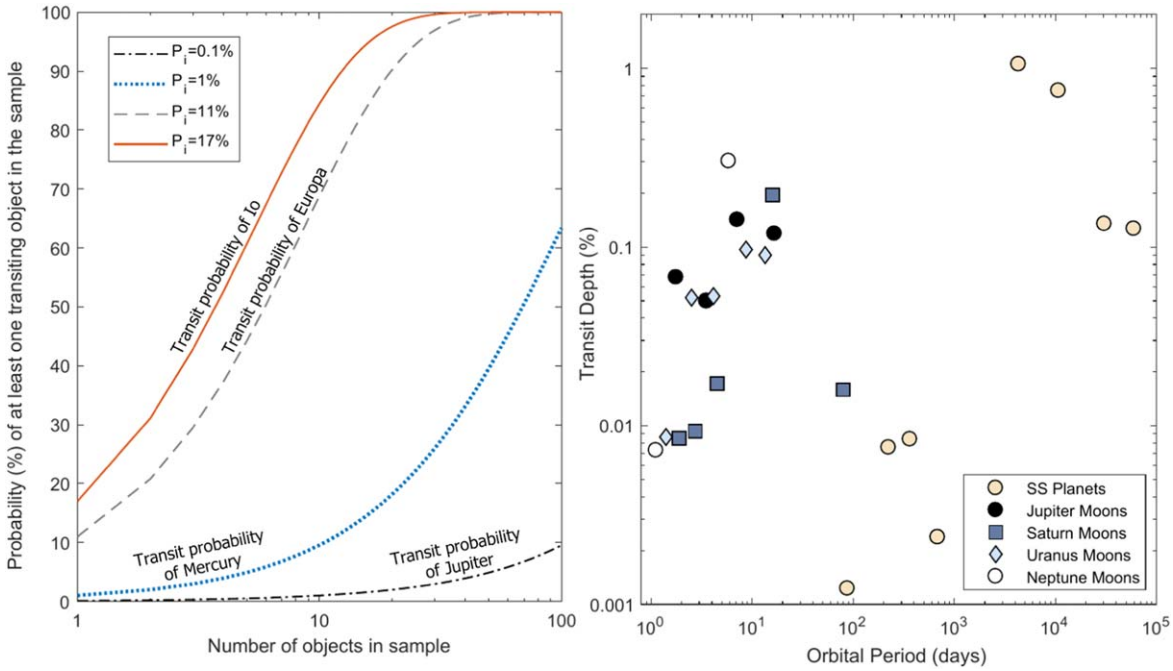

Figure 2. Left: probability that at least one transiting companion exists in a sample of N unrelated objects with identical secondary companions (Equation (1)). Different curves are for different choices of primary radius and orbital distance. The blue dotted line is for $R/a = 0.01$, similar to Mercury orbiting the Sun. The gray dashed curve is for $R/a = 0.11$, similar to Europa orbiting Jupiter. The red curve is for $R/a = 0.17$, similar Io orbiting Jupiter. The black dashed–dotted curve is for $R/a = 0.001$, similar to Jupiter orbiting the Sun. Right: transit depths and orbital periods for selected solar system moons orbiting solar system planets and solar system planets orbiting the Sun.

moon around a planet or a planet around a star based on solar system examples. About six solar system moons have transit depths comparable to those of Neptune and Uranus.

2.1.2. Transit Probability and the Roche Orbital Distance

Large moons must orbit exterior to the Roche orbital radius. Here we determine transit probabilities for secondaries that are

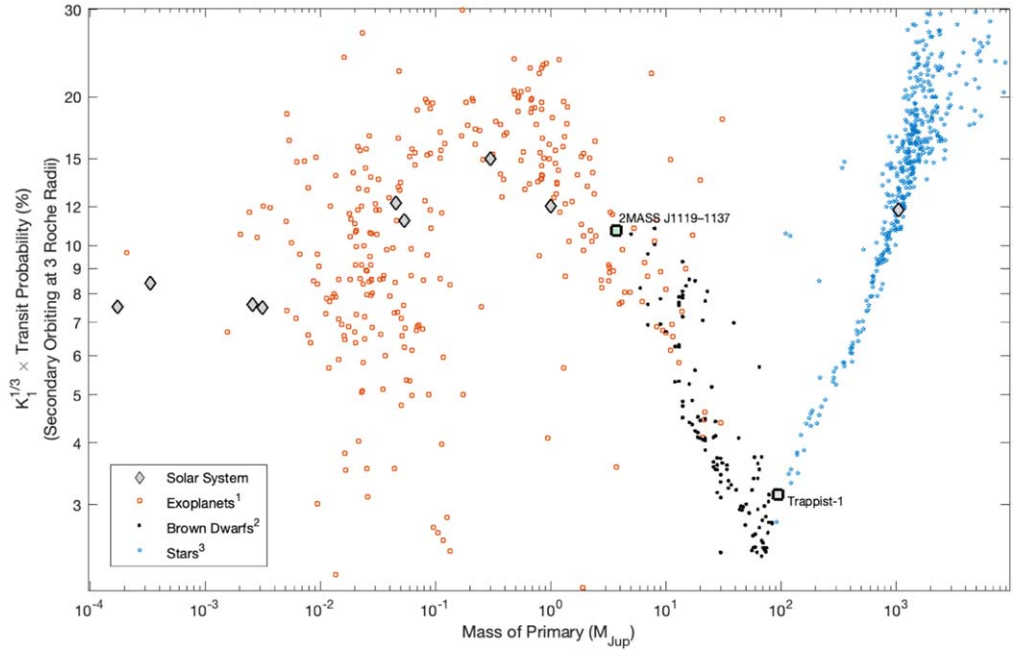

Figure 3. Geometric transit probability vs. primary mass, assuming a secondary companion orbiting at 3 Roche radii with a density of K_1 g cm^{-3}. The transit probability has a local maximum for gas giant planets because of their large radii and low densities. The diamonds represent the cases in which the primary object is a planet in the solar system or the Sun. Data were taken from (1) the NASA Exoplanet Archive (only objects with $a > 0.1$ au are included in this plot), (2) Gelino et al. (2009) and Southworth (2014), and (3) Parsons et al. (2018), and Best et al. (2020).

located at a fixed multiple of the Roche radius. The Roche radius for a body comprised of an incompressible fluid in a circular orbit is

$$d \simeq 2.44\, R_M \left(\frac{\rho_M}{\rho_m}\right)^{\frac{1}{3}}, \tag{2}$$

where R_M is the primary's radius and ρ_M and ρ_m are the densities of the primary and secondary, respectively (Roche 1849). We will consider moons for which $a = 3d$. This value was chosen because it is close to the mean separation between solar system gas giants and their closest large moons ($a = 3.2d$). Setting the density to a constant, K_1 g cm^{-3} for the secondary object, the transit probability at a fixed multiple of the Roche distance depends only on the properties of the primary object. Figure 3 shows the transit probability versus primary mass assuming a secondary companion orbiting at 3 Roche radii with a density of K_1 g cm^{-3}. To make this figure, we used data for the masses and densities of primary objects ranging from small rocky planets to O-type stars. For these calculations, we assume a random orientation, which may not be valid when additional geometric information is available, such as the orientation of the planet's orbit.

Starting from the mass of a small rocky planet, as the primary's mass is increased, the transit probability rises (with a large dispersion) until it reaches a local maximum in the vicinity of the gas giant planets. As the primary mass increases further, the transit probability plunges because the primary's radius remains roughly constant and the density increases, moving the Roche radius away from the primary. The most favorable transit targets in this sense are Saturn-mass objects. Specifically, the transit probability at $a = 3d$ is 10 times larger for a 0.4 $M_{\rm Jup}$ planet than it is for a 0.08 $M_\odot$ star. Furthermore, young IPMOs and brown dwarfs are often inflated (Baraffe et al. 2015). For these extremely low density objects, which typically have a radius of up to 1.5 $R_{\rm Jup}$, the transit probability at a given multiple of the Roche distance is even higher.

It is also noteworthy that 3 Roche radii corresponds roughly to the location of the habitable zone (HZ) around young IPMOs with effective temperatures of approximately 1000 K. Figure 4 is similar to Figure 3 but shows the transit probability of a secondary companion orbiting in the HZ instead of at 3 Roche radii. For this calculation, the HZ was taken to be the orbital distance at which the secondary receives the same bolometric flux from the primary as Earth does from the Sun. Starting from a solar mass, as the primary mass is decreased, the HZ transit probability rises until it reaches a plateau of 2% for M dwarfs. In the regime of brown dwarfs and IPMOs, the HZ transit probability resumes increasing again until the primary's luminosity is so low that the HZ is located within the Roche distance. In the solar system, the closest-in moons are at $a/R_{\rm p} \approx 4$ or approximately 2.2 Roche radii (e.g., Enceladus), corresponding to a transit probability of ≈25%. Thus, the region of Figure 4 with transit probabilities $\gtrsim$25% may be unrealistic, because we do not find moons in the solar system in such orbits.

2.2. Expected Exomoon Masses and Transit Depths

Most of the solar system moons are thought to have formed via accretion in a circumplanetary disk (Mosqueira & Estrada 2003). The typical moon-to-planet mass fraction for large moons is observed to be approximately 2.5×10^{-4}, which in theory is the result of the balance between the inflowing material and loss of material through orbital decay (Canup & Ward 2006). The *N*-body simulations have been used to study solar system moon formation and predict the demographics of exomoon systems (Ogihara & Ida 2012; Heller et al. 2014; Heller 2016; Miguel & Ida 2016; Moraes et al. 2018; Cilibrasi et al. 2018, 2021; Ronnet & Johansen 2020; Inderbitzi et al. 2020). In particular,

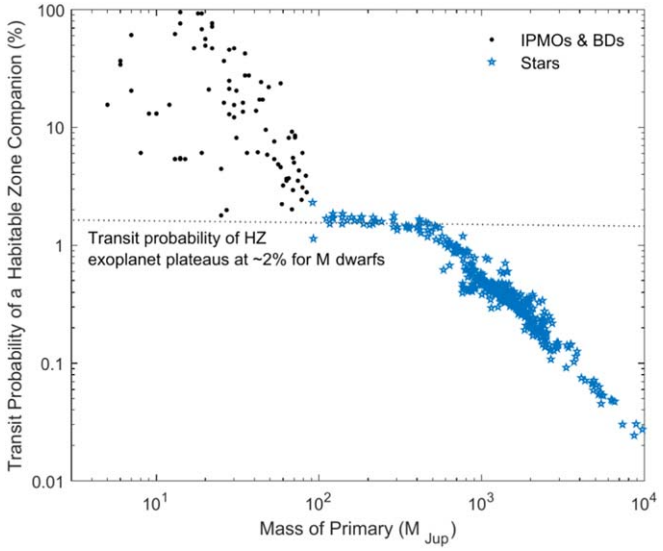

Figure 4. Transit probabilities of a companion in the HZ. Here we define the HZ as a companion receiving the same amount of flux as Earth. The transit probabilities of HZ companions are ∼2% for M dwarf exoplanets. For more massive stars, the HZ exoplanet transit probability decreases. Transit probabilities for brown dwarfs and IPMOs increase with decreasing mass until the primary becomes so cold that a companion can no longer stably orbit in the primary's HZ. Very low mass brown dwarfs and young IPMOs are the most likely objects to host habitable transiting companions. References: brown dwarfs and IPMOs, Gelino et al. (2009), Best et al. (2020); stars, Parsons et al. (2018), Southworth (2014).

Cilibrasi et al. (2018) used *N*-body simulations to show that the integrated moon mass of a Jupiter-like planet has a peak between 10^{-4} and 10^{-3} of the planet's mass, with an upper limit of about 0.1.

If IPMOs host moons with similar mass ratios, then based on these findings, we expect most IPMO systems to have multiple moons with mass 10^{-4}–$10^{-3}\,M_{\rm planet}$, transits of which could be detectable with JWST or other large infrared-equipped telescopes. For example, for an IPMO with mass $10\,M_{\rm Jup}$, a mass ratio of a few times 10^{-4} corresponds to an Earth-mass moon, and therefore it is reasonable to speculate that Earth-mass moons may be a common outcome of moon formation around IPMOs. Similarly, using the same mass ratio, the analogs of the Galilean satellites around a hypothetical $13\,M_{\rm Jup}$ IPMO would all be more massive than Mars.

2.2.1. Exomoon H/He Envelope Capture

For the preceding calculations, we assumed that the mass–radius relationship for exomoons is the same as observed for solar system moons and rocky exoplanets, which seems reasonable but need not be the case in reality. All of the currently detected rocky exoplanets have host stars older than 100 Myr. However, most of the known IPMOs are younger than 100 Myr. Many of the known short-period rocky exoplanets are thought to have once had a hydrogen–helium envelope constituting a few percent of the total mass, based on theoretical interpretations of the dip at $2\,R_\oplus$ in the observed radius distribution (also called the "radius valley"; Lopez & Fortney 2014; Fulton et al. 2017; Owen & Wu 2017; Owen 2020; Misener & Schlichting 2021; Rogers & Owen 2021). In these theories, close-orbiting planets below a certain mass threshold are liable to losing their gaseous envelopes over tens to hundreds of megayears due to high-energy radiation from the primary star or core-powered mass loss (Rogers et al. 2021). Planets as small as Mars ($\gtrsim$0.1 $M_\oplus$) are thought to be sufficiently massive to initially capture H/He during formation (Hayashi et al. 1979; Erkaev et al. 2014; Stökl et al. 2015, 2016). Cilibrasi et al. (2021) found that the moons form on a timescale of 10^5 yr. The envelope mass fraction of a 1 $M_\oplus$ core after being embedded in a disk for 10^5 yr is 1.4% (Stökl et al. 2016), which is a sufficient mass fraction for substantially increasing the radius of the object (Rogers et al. 2011; Mordasini et al. 2012). Although this estimate is given for relevant moon formation timescales, simulations are for disk conditions (temperature and density) consistent with a planetary nebula at 1 au around a Sun-like star. Further modeling, beyond the scope of this paper, is needed to understand how envelope capture would differ for the gas temperatures and densities expected in the circumplanetary disk of an IPMO. If similar results hold, one might expect large young moons to have H/He envelopes similar to young planets, which would significantly increase their radii and transit depths. According to this analogy, a young Earth-mass moon might have a radius of $2\,R_\oplus$. Earth-sized moons with H/He envelopes transiting young IPMOs would be less challenging to detect due to exceptionally large transit depths, in the neighborhood of 2%.

In summary, based on our analogy with the solar system and on moon formation simulations, it is reasonable to expect that $\gtrsim$80% of $10\,M_{\rm Jup}$ IPMOs are hosts of multiple moons that produce transit depths $\gtrsim$0.1% if the geometry of the system is favorable (Cilibrasi et al. 2021). This is in contrast to what is observed in the exoplanet population. The results of the Kepler mission demonstrated that planets with such large transit depths and periods shorter than a few days are rare (Beaugé & Nesvorný 2012; Sanchis-Ojeda et al. 2014; Mazeh et al. 2016), and hot Jupiters have long been known to have an occurrence of 1% or lower (Wright et al. 2012; Zhou et al. 2019). In short, there is no known reason to think there is a "close-in large moon desert" akin to the "hot Neptune desert" and the low occurrence of hot Jupiters.

2.3. Orbital Periods and Transit Durations

The orbital periods of exomoons are similar to those of hot Jupiters and shorter than those of the solar system planets or typical exoplanets in the observed sample. Short periods correspond to higher transit probabilities and are also helpful for transit detection by reducing the required amount of observing time to catch multiple transits. Heller (2016) calculated that the large moons of the solar system transit at an average frequency of 0.17 day^{-1}. By performing a similar calculation, we find that the median transit frequency for the closest large moon orbiting each solar system gas giant planet is 0.55 (using Io, Tethys, Miranda, and Triton) or 0.63 (if we replace Triton with the closer, lower-mass moon Proteus) transits day^{-1}. Assuming exomoons have orbital periods similar to the solar system moons,[10] this implies that, on average, we need only observe a IPMO for a couple of days in order to achieve sufficient temporal coverage to detect transiting moons.

Figure 5 shows the relationship between exomoon orbital distance, orbital period (left), transit duration (right), and the probability of exomoon detection. For an edge-on exomoon system, the transit durations are a few hours. Based on our discussion of transit probabilities in Section 2.1.1, most planets will have a moon with a transit probability of 10%–20%,

[10] This assumption is roughly consistent with our earlier assumption that moons form at a typical multiple of the Roche distance, because at a fixed orbital period, the Roche distance depends only on the mean density of the moon (Rappaport et al. 2013).

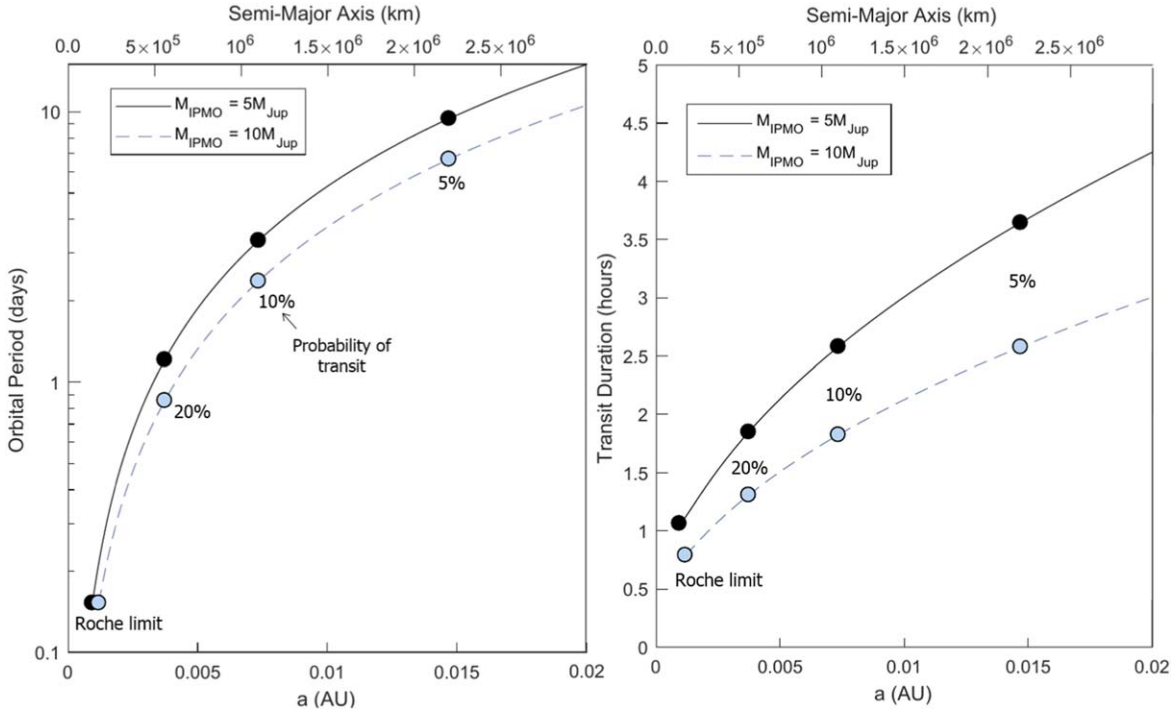

Figure 5. Orbital period (left) and transit duration (right; assuming $i = 90°$) vs. orbital distance for IPMOs of mass 5 (solid curve) and 10 (dashed curve) $M_{\rm Jup}$, in both cases with radius 1.5 $R_{\rm Jup}$. The circles and labels indicate the corresponding transit probabilities and the Roche limit. Based on the left panel, an observation of a 10 $M_{\rm Jup}$ planet lasting 20 hr is required to detect all of the exomoons with transit probabilities >20% ($a < 0.004$ au). Based on the right panel, the exomoons with transit probabilities >20% have transit durations of 1–2 hr.

corresponding to an orbital distance of $\sim 10^6$ km (0.007 au). Based on Figure 5, this implies that if an exomoon is transiting the planet, it will likely be detected within ~50 hr of observations. Thus, if one were interested in surveying planets for transiting exomoons, a minimum of ~50 hr per target would suffice. Experience has shown that detecting transiting exoplanets requires surveys of hundreds or thousands of stars for an interval of at least a few weeks or months. Although wide-field observations of hundreds of IPMOs are not currently possible, there are still good prospects for detecting transiting moons of IPMOs with a few days of observations for each of dozens of objects.

3. Detectability

3.1. Ground- and Space-based Observations

When trying to detect a transiting moon, the main advantage of IPMOs over other directly imaged planets is that high-contrast, high angular resolution imaging is not required. Using high-contrast imaging techniques, it has proven difficult to achieve a photometric precision better than the 1% level in 1 hr due to photon noise from the host star and time-variable image artifacts (Sahoo et al. 2020). For example, attempts have been made to search for variability of the HR 8799 planets, but the upper limits on any variability are only at the 5%–10% level (Apai et al. 2016; Biller et al. 2021).

In contrast, very high photometric precision (200–500 ppm) within a factor of 2 of the photon limit has been achieved for isolated point sources using near-infrared cameras on ground-based telescopes (de Mooij & Snellen 2008; Sada et al. 2010). The current sample of IPMOs is bright enough ($K \sim 14.5$, $J \sim 16.5$ mag) to support a photon-limited precision of ~0.1% (1000 ppm) in 1 hr with a large (8–10 m) telescope. For example, a typical near-infrared imager[11] on an 8 m telescope has a photon-limited *Ks*-band precision of about 750 ppm in 1 hr at $K = 14.5$ (15 s exposures, 1 hr of total observation time including overheads). Even if the achievable precision is a factor of 2 worse than the photon limit, this would be sufficient for a 6σ detection of a 1 hr transit of an Earth-sized moon around a Jupiter-sized planet. Detection of super-Earth and Neptune-sized moons should be possible with 2 m class telescopes. For example, Tamburo & Muirhead (2019) showed that a large survey of L and T dwarfs with a small ground-based telescope is likely to detect at least one transiting planet. They are using this strategy to conduct the Perkins INfrared Exosatellite Survey (PINES) in search of transiting companions around L- and T-type brown dwarfs.

With JWST, because of the low sky background and stable platform, it should be possible to improve the photometric precision by an order of magnitude compared to ground-based observatories. It will likely be easier to approach the photon limit with JWST than with ground-based telescopes, as proved to be the case for Hubble Space Telescope (HST) and Spitzer observations. Figure 6 compares the detection limits of various instruments and exomoon detection methods.

Using the JWST/ETC,[12] we estimated the expected JWST NIRSpec photometric precision (JNSPP) and minimum detectable moon radius for the 57 IPMOs or candidate IPMOs listed Table 1. Spectral imaging is preferred over imaging because the dispersed light allows for longer exposures and lower overheads. For transit detection, the total flux signal would initially be more important than the spectral information. The spectral information would be useful to check for

[11] Gemini/Flamingos-2 Exposure Time Calculator.
[12] jwst.etc.stsci.edu

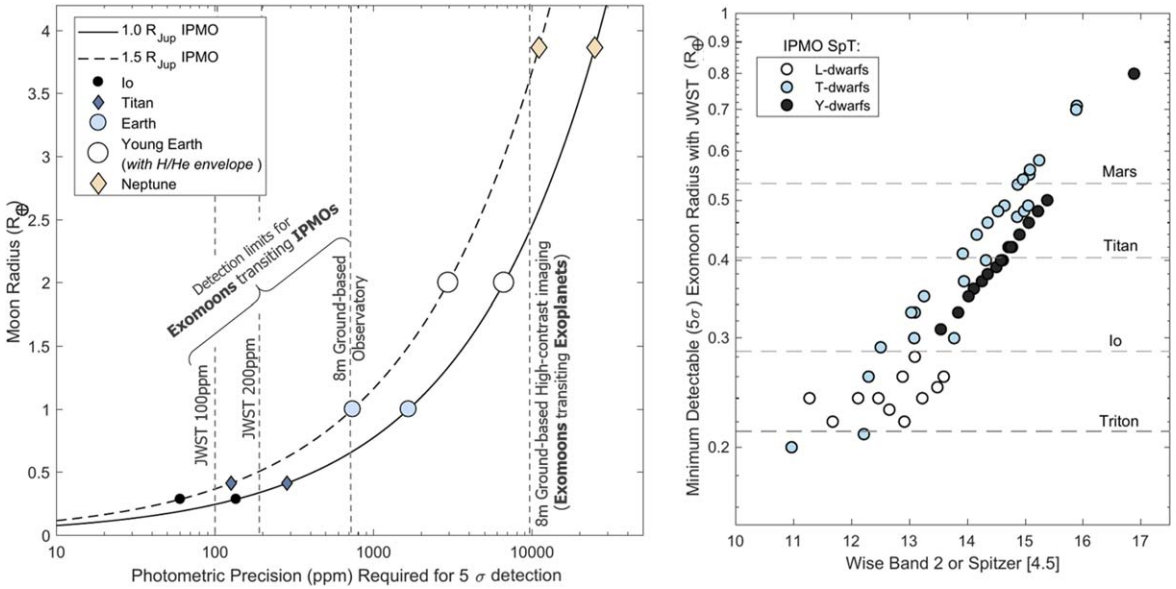

Figure 6. Left: photometric precision required for a 5σ detection of a transiting exomoon as a function of the exomoon's radius, assuming the planet's radius is 1.0 (solid black line) or 1.5 (dashed black line) $R_{\rm Jup}$. Calculations assume a single 1 hr transit with a JNSPP of 100 or 200 ppm, achievable on 17 or 30 of the 57 IPMOs listed in Table 1, respectively. Vertical dashed gray lines show the photometric sensitivity of various observatories/methods. The JWST can detect analogs of the large moons in the solar system, and ground-based observatories can detect Earth-sized exomoons. Neptune-sized exomoons transiting directly imaged exoplanets are detectable with high-contrast imaging systems. Earth-sized moons with H/He envelopes (white dots) are more easily detected than purely rocky Earths (pale blue dots). Right: minimum detectable exomoon radius as a function of WISE Band 2 magnitude (or Spitzer [4.5] if WISE magnitude is unavailable) for IPMO calculations given in Table 1. Titan-sized moons are detectable around most IPMOs.

achromaticity of any flux dips (as would be expected of transit events), as well as to characterize the planet's own spectrum and intrinsic variability. This is discussed in more detail in Section 3.2.

We used the following process to calculate the JNSPP and minimum detectable exomoon radius. We note that the assumptions used in this calculation are approximate for individual objects but representative of the expected exomoon detection limits for the currently known IPMO population as a whole. However, more precise estimates using models tailored to the exact spectral energy distribution and physical parameters of each IPMO will result in more accurate exomoon detection limits at the individual IPMO level.

1. Select an IPMO model from the Sonora 2018 grid (Marley et al. 2018) based on the spectral type. The IPMOs are grouped into five bins/models—early L (L0–L4.5): 1700 K model, late L (L5–L9.5): 1200 K, early T (T0–T4.5): 900 K, late T (T5–T9.5): 600 K, and early Y: 350 K—based on Filippazzo et al. (2015). These five spectral models were uploaded to the JWST/ETC for S/N calculations.
2. The uploaded model is renormalized to the magnitude of each target at 4.5 μm (or in the K band when a 4.5 μm flux is unavailable).
3. Using the JWST/ETC, the S/N in the NIRSpec bright object time series (BOTS) prism (low-res) mode is calculated for each target. This observing mode is used because it allows spectral coverage from 0.6–5 μm, so no adjustment of the bandpass is needed as the spectral type/temperature of the IPMO varies. Because of the unprecedented stability of JWST and NIRSpec's large slit size ($1\farcs6 \times 1\farcs6$), NIRSpec will likely be able to achieve near photon-limited precision. However, if slit losses are a concern or a reference star is needed, simultaneous NIRCam long-wave slitless grism mode + short-wave defocused imaging results in comparable photometric precisions on IPMOs. The detector setup and exposure time are optimized to provide the maximum S/N while avoiding saturation. Note that in a few cases, the rapid readout pattern was required to avoid saturation, which increased the overhead and decreased the S/N on the brightest IPMOs. In all cases, we require the cadence to be <1 minute, such that there is sufficient time resolution to observe a transit. The total observation time is set to 1 hr, and the SUB2048 array is used for all calculations.
4. The total S/N from the sum of all flux over the entire spectral range (0.6–5.3 μm) is then computed and converted to the JWST NIRSpec 1 hr photometric precision (JNSPP-1hr) in ppm. This value is given for each target in Table 1.
5. The minimum detectable moon radius is calculated from the JNSPP for each target using a simple box approximation for the transit. For this calculation, we assume that the host is 1.3 $R_{\rm Jup}$ if it is a moving group association member/candidate and presumably young, which typically corresponds to a larger IPMO radius. For field IPMOs, which are typically older, we assume a radius of 1.0 $R_{\rm Jup}$. It is worth noting that for all objects with masses in between those of Saturn and low-mass stars, the radius is generally confined to the narrow range of 0.9–1.5 $R_{\rm Jup}$. The 5σ minimum detectable moon radius ("limit") is given in $R_{\rm Titan}$ and $R_\oplus$ in Table 1.

Based on these calculations, we find that of the 57 IPMOs listed in Table 1, Europa-sized moons are detectable around 11 IPMOs; Ios around 16; Titans or Ganymedes around 33, which is more than half of all known IPMOs; and Mars around 49, and Earth-sized moons are detectable around all 57 IPMOs with S/N $> 5\sigma$ in 1 hr with JWST/NIRSpec.

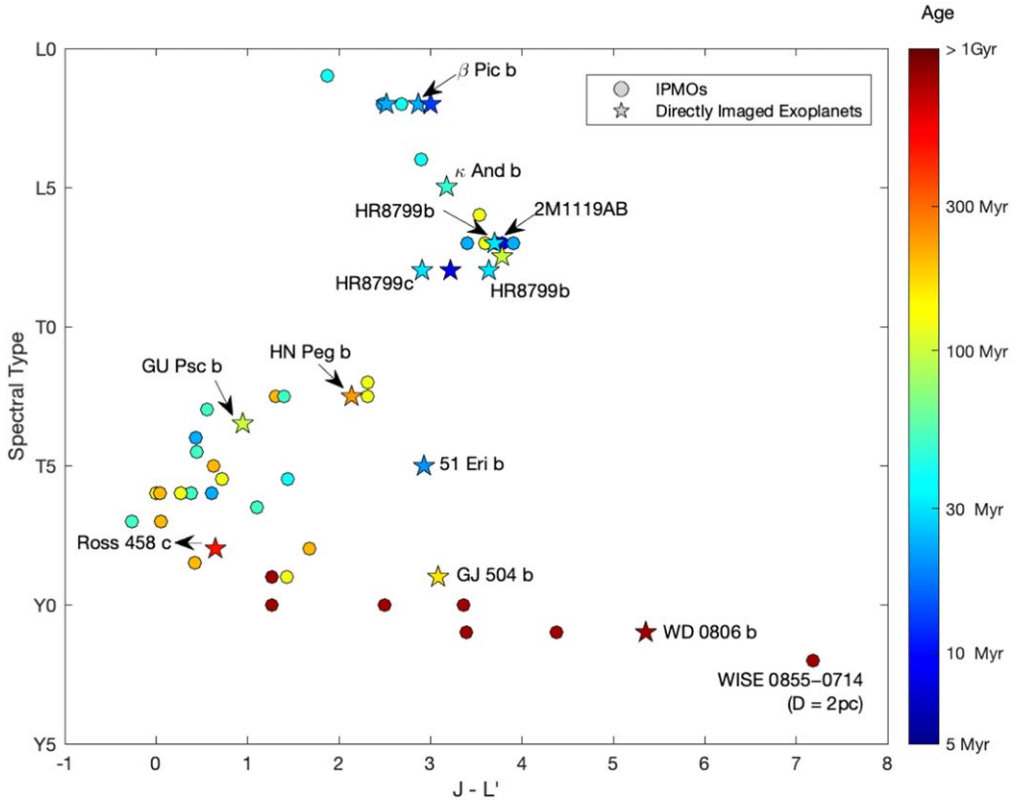

Figure 7. Color vs. spectral type for directly imaged exoplanets and IPMOs. All of the plotted objects have estimated masses between 1 and 13 $M_{\rm Jup}$. An object's position on this plot is typically set by both age and mass. The hotter L–T objects are generally members of young moving groups, which constrains their masses to be in the planetary regime. The Y dwarfs have not been identified as moving group members, but due to their cold temperatures, they lie in the planetary-mass regime regardless of age. The directly imaged exoplanets and IPMOs appear similar, suggesting that they may also have similar satellite systems. Note the similarities between the planets around HR 8799 and the IPMO 2MASS J1119–1137AB. In constructing the color, the L′ magnitude was used for directly imaged planets, whereas the WISE band 1 or Spitzer [3.6] band was used for IPMOs when L′ was not available. References: NASA Exoplanet Archive; Best et al. (2020).

While the detection of such small (Galilean-sized) moons should, in theory, be possible for many IPMOs with JWST, this level of sensitivity would not be required if moon masses were proportional to planet masses ($M_{\rm moons} \approx 2 \times 10^{-4}\ M_{\rm planet}$; Canup & Ward 2006). In this scenario, a typical 10 $M_{\rm Jup}$ IPMO would have moons with sizes in between those of Titan and Earth. As we demonstrated, moons in this mass range should be detectable around almost all known IPMOs.

Table 1 provides a list of 57 IPMOs or candidate IPMOs drawn from the literature. We did not include objects that were slightly above the 13 $M_{\rm Jup}$ cutoff, even if their error bars (due to an uncertainty in age) indicated that they may be of planetary mass; e.g., 2MASS J1324+6358 (Gagné et al. 2018), a $13.2^{+1.8}_{-1.3} M_{\rm Jup}$ object, was excluded from this list, as it is slightly more probable that it is a brown dwarf rather than an IPMO. As previously noted (Faherty et al. 2016; Liu et al. 2016), IPMOs and directly imaged exoplanets occupy the same ranges of effective temperature, age, and mass (see Figure 7). It is plausible that these two sets of planetary-mass objects have exomoons with similar properties. We prepared this table and figure to convey the typical magnitudes and other properties of IPMOs and allow for the assessment of exomoon detectability. The IPMOs range in magnitude from 11 to 16 in the WISE 4.5 μm band. Based on the statistics described in Section 2, if exomoons existed around all of these systems, and we observed each one for 2 days with JWST, we would expect several detections. If no exomoons were detected, we would be able to place meaningful upper limits on exomoon occurrence that would inform our understanding of IPMOs, exomoon formation, and exomoon survivability during planet ejection (Hong et al. 2018; Rabago & Steffen 2018).

For the L and early T dwarfs brighter than $K \approx 15$, exomoon transit searches are possible with ground-based K-band observations. For the planetary-mass Y and late-type T dwarfs, transit searches are probably only feasible by observing further in the infrared range with JWST. However, although Y-dwarfs are typically fainter and have lower JNSPP, they are also generally smaller in radius because they are older. This smaller radius allows for the detection of moons similar in size to younger IPMOs with JWST despite their faintness. For example, the Y dwarf WISE 1541–2250 is at a distance of 6 pc and has a WISE 4.5 μm band magnitude of 14, despite being more than a gigayear old (Kirkpatrick et al. 2012), allowing for detection of Titan-sized moons around this IPMO.

3.2. Substellar Variability

The atmospheres of solar system gas giants, giant exoplanets, and brown dwarfs are characterized by complex chemical processes that often lead to the formation of clouds. The result is rotationally modulated flux variability produced by cloud features rotating in and out of view. In the case of Jupiter, unresolved observations at 5 μm revealed periodic variability with amplitudes exceeding 20% (Gelino & Marley 2000; Ge et al. 2019). Both isolated and companion substellar objects are

known to exhibit photometric and spectroscopic variability across the full L–Y spectral sequence. This variability probably poses the greatest obstacle to detecting exomoon transits. Large variability surveys from the ground and space have revealed that photometric variability is common in field brown dwarfs (Buenzli et al. 2014; Radigan et al. 2014; Metchev et al. 2015). Recent studies have also suggested that variability may be enhanced for the low-gravity brown dwarfs and IPMOs considered here (e.g., Schneider et al. 2018; Vos et al. 2019, 2020). Typical infrared amplitudes range from 0.1% to 5%, although variations as large as 25% were observed for the $\approx 13\,M_{\rm Jup}$ isolated object 2MASS J21392676+0220226 (Radigan et al. 2012) and the $\approx 20\,M_{\rm Jup}$ companion VHS J1256–1257b (Bowler et al. 2020; Zhou et al. 2020). The variability of Y dwarfs has not yet been studied in great detail, but initial results suggest that they exhibit significant non-sinusoidal variability (Cushing et al. 2016; Esplin et al. 2016; Leggett et al. 2016). Therefore, we should expect the amplitude of intrinsic variations to be on the same order of magnitude (or higher than) the transit signals.

If the periodic variations of the planet remain stable over many cycles, it may be possible to derive an accurate model for intrinsic variations and isolate any transit signals. For example, the light curves of the brown dwarfs WISEP J190648.47+401106.8 and 2MASS J10475385+2124234 remained stable over many rotations (Gizis et al. 2015; Allers et al. 2020). However, other brown dwarfs have light curves that evolve on rotational timescales, most notably in several L/T transition brown dwarfs such as 2MASS J13243553+6358281, SIMP J01365662+0933473, and 2MASS J21392216+0220185 (Apai et al. 2017). In such cases, it will be more difficult to identify a transit. Atmospheric dynamical models have shown that light-curve evolution is likely very common for brown dwarfs and exoplanets (Tan & Showman 2021), but relatively few objects have been monitored longer than ~20 hr. In contrast to evolving cloud-driven variability, the transit signal from an exomoon would have a consistent depth and duration. Thus, long-term monitoring and searching for repeatable periodic transit signals will be important. Such a search could be done for a handful of brown dwarfs that are bright enough to be observed by the Transiting Exoplanet Survey Satellite (e.g., Ricker et al. 2015; Apai et al. 2021), but an infrared monitoring campaign would be necessary for a large-scale search for transiting moons.

Another possibility for disentangling intrinsic variations from transits is with spectral time series. There have been many multiwavelength studies of variability in brown dwarfs and planetary-mass objects. Spectroscopic monitoring using the HST WFC3 grism camera in particular has revealed the spectral signatures of cloud-driven variability in the atmospheres of both brown dwarfs and planetary-mass objects (Apai et al. 2013; Biller et al. 2018; Lew et al. 2020). Such signatures sometimes include wavelength-dependent phase shifts due to clouds at different layers in the atmosphere (Buenzli et al. 2014; Biller et al. 2018). For example, Biller et al. (2018) observed phase offsets ranging from 200° to 210° between simultaneously observed light curves from HST and the Spitzer Space Telescope for the free-floating planetary-mass object PSO J318.5–22. Such phase shifts would not occur for a signal due to a transiting exomoon. Additionally, many studies have characterized the wavelength dependence of the variability amplitude for L–T objects (see Manjavacas et al. 2019, for a compilation). The spectral signatures of an exomoon transit are likely to differ from the signatures of clouds that have already been characterized in the literature.

Despite the additional complications arising from substellar variability for an exomoon search, the existence of variability in a target can have its advantages. By combining rotation periods with high-resolution spectra (from which the projected rotation velocity can be measured), it is possible to derive a constraint on the viewing inclination for variable brown dwarfs and exoplanets (e.g., Vos et al. 2017, 2020). Assuming the moon's orbit is aligned with the planet's rotational axis, this would allow transit surveys to avoid pole-on systems, thereby increasing the average transit probability of the observed targets (see Beatty & Seager 2010, for a discussion of the application of this idea to transiting planets). For example, an Io transit of a Jupiter-sized planet is observable for inclinations between 79.°5 and 90° (see Figure 1), giving a geometric transit probability of $\cos(79.^\circ5) \approx 0.18$. If it were possible to exclude systems with inclinations lower than 60° based on prior observations that constrained the IPMO's inclination, the geometric transit probability would double, becoming $\cos(79.^\circ5)/\cos(60^\circ) \approx 0.36$. In this respect, β Pic b offers a particularly favorable geometry for the detection of transiting moons. If it has a close-in moon system aligned with the star–planet inclination of 89° (Kraus et al. 2020), transits are guaranteed. For the favorable case of an Earth-mass moon with a H/He envelope, the transit signals would have an amplitude of about 2%, which might be barely detectable with existing ground-based high-contrast imaging instrumentation.

3.3. Simulated Exomoon Transits

To illustrate the capability of JWST to detect transiting exomoons around IPMOs, we simulated the light curves of two exomoons transiting a $1\,R_{\rm Jup}$ IPMO using Starry (Luger et al. 2019). We generated a transit light curve for an Earth-sized moon with a radius of $1\,R_\oplus$, an orbital period of 3 days, and a transit duration of 1.3 hr. We also generated a light curve for a Titan-sized moon with a radius of $0.404\,R_\oplus$, an orbital period of 1 day, and a transit duration of 1 hr in the same synthetic data set (see Figure 8). The noise was assumed to follow a Gaussian distribution with a standard deviation set by the expected sensitivity of the JWST NIRSpec BOTS mode (a JNSPP-1 hr of 100 ppm or a photometric precision of 350 ppm per 5 minute bin). This results in a 97σ detection of each transit of the Earth-like exomoon (duration 1.3 hr, depth 0.8%) and a 13σ detection of each transit of the Titan-like exomoon (duration 1 hr, depth 0.13%).

The goal of this calculation is simply to illustrate that JWST has sufficient sensitivity to detect exomoons and to demonstrate the expected level of photon noise in those observations. In reality, observations will likely be limited by variability in the IPMO. The extent to which variability will hinder exomoon detection is currently poorly understood. Section 4 provides an example showing real IPMO variability in two different photometric bands of Spitzer light curves. This example illustrates how variability impedes exomoon detection. It also shows how the IPMO variability differs between photometric bands, which demonstrates how we may be able to use spectral information to differentiate between chromatic IPMO variability and (almost) gray exomoon transits. Untangling the spectrally resolved, time-domain variability of IPMOs from exomoon transits in JWST light curves will require complex

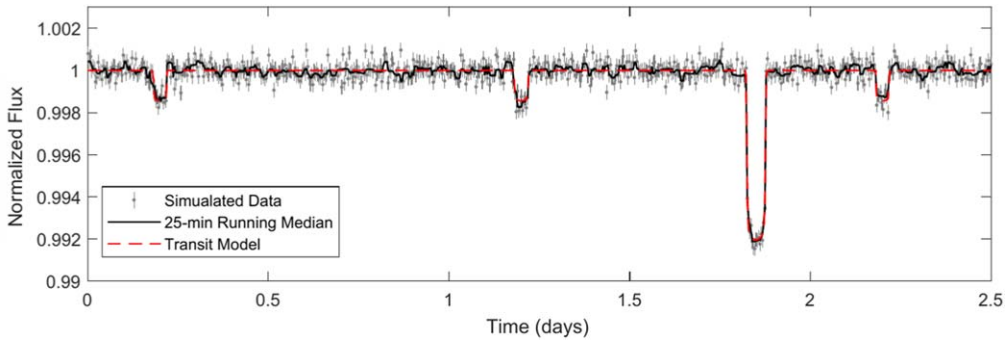

Figure 8. Simulated transits observed with JWST/NIRSpec of Earth- and Titan-sized exomoons transiting a 1 $R_{\rm Jup}$ IPMO. The transiting Earth- and Titan-sized exomoons are detectable at 97σ and 13σ, respectively.

IPMO variability modeling coupled with exomoon transit models.

4. A Fading Event for 2MASS J1119–1137AB

As a proof of concept, we use existing Spitzer light curves to demonstrate how this exomoon detection method might work and illustrate some of the challenges of the technique.

4.1. A Binary IPMO

The binary IPMO 2MASS J1119–1137AB has nearly identical, equal-brightness giant planets separated by $3.9^{+1.9}_{-1.4}$ au with an orbital period of 90^{+80}_{-50} yr (Best et al. 2017a). The source is known to be an equal-brightness binary based on Keck AO observations in 2016, which gave (Best et al. 2017a)

$$\log\left(\frac{L_{\rm bol,A}}{L_\odot}\right) = -4.73^{+0.27}_{-0.21} \text{ and}$$
$$\log\left(\frac{L_{\rm bol,B}}{L_\odot}\right) = -4.74^{+0.27}_{-0.21}. \quad (3)$$

For our analysis below, we assumed that the two components have equal flux. The system is a candidate member of the TW Hydrae association (Kellogg et al. 2016; Best et al. 2020a). If the binary is a member of TW Hya, then evolutionary models predict that the mass of each planet is $3.7^{+0.9}_{-1.2}$ $M_{\rm Jup}$ assuming a system age of 10 ± 3 Myr (Best et al. 2017a). If the system is not associated with TW Hya, then it is likely older (10–100 Myr), and the estimated mass of each planet is $9.2^{+1.9}_{-2.3} M_{\rm Jup}$ (Best et al. 2017a). In either case, the masses are consistent with planetary-mass substellar objects. Whether it is associated with TW Hya or not, the spectrum of 2MASS J1119–1137AB was classified as very low gravity, a signature of youth implying that the binary is young and has low-mass components (Best et al. 2017a).

Based on the possibility that 2MASS J1119–1137AB is a relatively isolated member of the TW Hya association, Best et al. (2017a) argued that the system is a product of normal star formation processes, rather than having been ejected via dynamical interactions from a higher-order system. More recent work (Best et al. 2020a) argues that 2MASS J1119–1137AB is older and unassociated with TW Hya, in which case its history might have included ejection from a star system. Simulations by Reipurth & Mikkola (2015) demonstrated that dynamical interactions in triple systems naturally lead to a population of free-floating brown dwarf binaries; however, the simulations did not include objects lower in mass than 12 $M_{\rm Jup}$. Detection of the orbital motion of the two IPMOs would lead to constraints on the masses and thereby shed light on their ages and formation mechanisms.

Schneider et al. (2018) observed 2MASS J1119–1137AB with the Spitzer Space Telescope to measure the rotation periods. We noted an intriguing brightness dip in the published light curve. As described below, we explored the possibility that this fading event is due to a transiting moon.

We briefly discuss the WISEA J1147–2040 IPMO light curve (Schneider et al. 2018) in the following analysis as a point of comparison. WISEA J1147–2040 is similar to 2MASS J1119–1137AB in age, distance, spectral type, and brightness. It is also a candidate member of TW Hya with an estimated mass of 5–13 $M_{\rm Jup}$, but it is not known to be a binary (Schneider et al. 2016).

4.2. Detection of a Fading Event

The Spitzer Space Telescope spent 20 hr (12 s exposures) observing 2MASS J1119–1137AB, split equally between the IRAC [3.6] and [4.5] μm bands. An identical observation was performed on WISEA J1147–2040. The IRAC pixel size was 1.″2, and the A and B components of 2MASS J1119–1137 were separated by 0.″14; thus, they were spatially unresolved. We used the A + B light curve produced by Schneider et al. (2018). The resulting light curve is shown in the top panel of Figure 9. For comparison, the WISEA J1147–2040 light curve is shown in Appendix B. WISEA J1147–2040 has a much longer rotation period (19.4 hr) compared to 2MASS J1119–1137 (Schneider et al. 2018).

To characterize the apparent fading event in the 2MASS J1119–1137 data set at the 8 hr mark, we fitted the light curve using two models.

1. A sinusoidal function, the most commonly used model for IPMO and substellar variability. There are four parameters: amplitude, phase, period, and mean flux.
2. A sinusoidal function with an inverted rectangular pulse. This "box" component adds three more parameters, the duration, midpoint, and depth of the box, for a total of seven parameters.

We implemented a Markov Chain Monte Carlo (MCMC) approach to find the best fit. For each fit we used 30 walkers, 15,000 steps, where the first 3000 steps were burn-in (the corner plot for the sine+box fit is shown in Appendix B). The fits to the 3.6 and 4.5 μm Spitzer data were done independently. We used the Bayesian information criterion (BIC) to determine

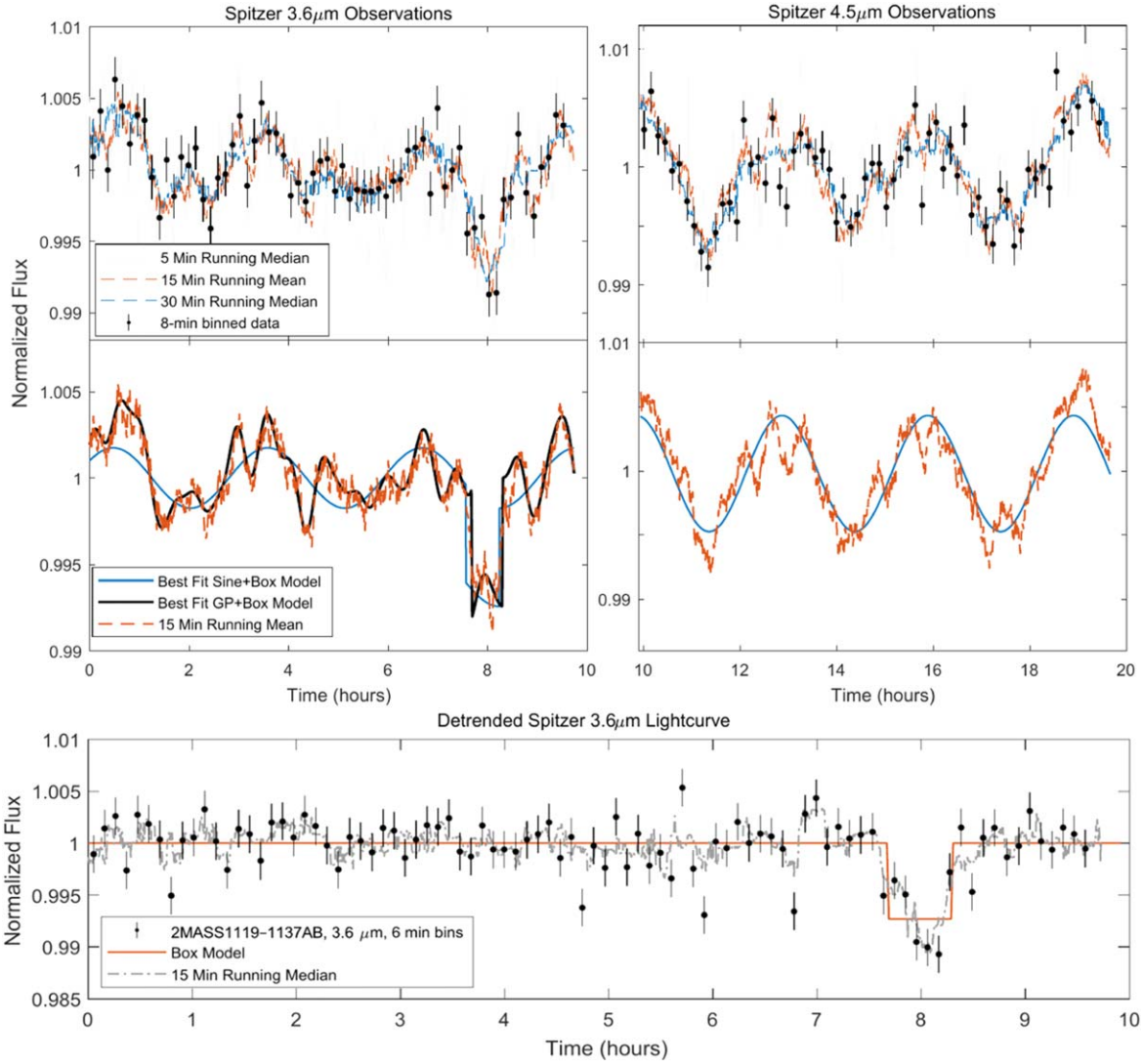

Figure 9. Top: Spitzer light curves of 2MASS J1119–1137AB based on a single 20 hr observation, 10 hr at 3.6 μm (left) and 10 hr at 4.5 μm (right). Note the fading event at the 8 hr mark of the 3.6 μm light curve. Middle: in addition to the 15 minute running mean of the data (red dashed line) are the best-fit sine+box model (blue curves) and the GP model of the 3.6 μm data (black curve). The sine+box model is favored over the sine-only model by ΔBIC = 22. The GP+box model is favored over the GP-only model by a Bayes factor of 3. Bottom: detrended (with GP fit) light curve and box fit to the data.

which model is best justified by the data. The BIC has been used in other studies to distinguish between variable and nonvariable models (Naud et al. 2017; Vos et al. 2020).

For the 2MASS J1119–1137AB 3.6 μm Spitzer light curve, of these two models, the sine+box was most preferred. We interpret this result as evidence that the fading event occurred. The sine+box model was preferred over the sine-only model with a ΔBIC = 22.2 indicating strong evidence for a fading event. The best-fit sine+box model (blue line) is shown in the middle left panel of Figure 9. We also attempted to fit a full transit model to the event, but the data did not provide enough information to constrain the impact parameter, limb-darkening coefficients, or other orbital parameters (if the event corresponds to an exomoon transit), and the sine+box model was preferred over the sine+transit model. We extracted the Spitzer light curve using a different pipeline (described in Vos et al. 2020). The sine+box model was still strongly favored despite the different light-curve extraction technique.

For comparison, we conducted the same analysis using the sine+box and sine fits of three other data sets: the 2MASS J1119–1137AB 4.5 μm Spitzer light curve and the WISEA J1147–2040 3.6 and 4.5 μm light curves. The light curves were generated using the methods described in Schneider et al. (2018). For these three data sets, we found that the sine+box model was ruled out and the sine-only model was preferred with ΔBICs of −4.0, −4.8, and −11.5, respectively, indicating that the anomalous event detected in the 2MASS J1119–1137AB 3.6 μm light curve is above the normal level of IPMO variability measured in the other three light curves.

Out of concern that the sine+box model is not realistic enough to model the planet's intrinsic variability, we also fitted the data with a Gaussian process (GP) model with and without a boxlike dip. Our GP analysis was similar to that presented by Van Eylen et al. (2018). In short, we employed a quasiperiodic kernel,

$$C_{ij} = h^2 \exp\left[-\frac{(t_i - t_j)^2}{2\tau^2} - \Gamma \sin^2 \frac{\pi (t_i - t_j)}{T}\right] + [\sigma_i^2 + \sigma_{\rm jit}^2]\delta_{ij}, \quad (4)$$

Table 2
Best-fit Box Parameters

Parameter	Sine+Box Model	GP+Box Model
$T_{\rm mid}$ (hr)	7.91 ± 0.03	7.94 ± 0.06
Duration (minutes)	38 ± 3	36 ± 6
Depth (%)	0.53 ± 0.05	0.63 ± 0.15
Depth ($R_\oplus$)	1.59 ± 0.14	1.74 ± 0.41

Note. The calculation of the depth in Earth radii assumes that both IPMOs have a radius of 1.38 $R_{\rm Jup}$ and the moon transits one of the two equal-flux, equal-radius (identical) planets.

Table 3
2MASS J1119–1137AB Variability Parameters

Parameter	This Work[a]	Schneider et al. (2018)
Mean flux	1.00175 ± 0.0003	0.9999 ± 0.0003
Amplitude (%)	0.17 ± 0.03	$0.230^{+0.036}_{-0.035}$
Period (hr)	$3.12^{+0.09}_{-0.08}$	$3.02^{+0.07}_{-0.06}$
Phase[b] (deg)	37 ± 15	29^{+16}_{-13}

Notes.
[a] Based on the best-fit sine parameters from the sine+box model.
[b] Rotational phase of the planet at $t = 0$.

where C_{ij} is the covariance matrix, δ_{ij} is the Kronecker delta function, h is the amplitude of the correlated noise, t_i is the time of the ith observation, τ is the correlation periodicity, Γ is the ratio between the squared exponential and periodic parts of the kernel, T is the period of the correlation, and $\sigma_{\rm jit}$ is a white-noise term in addition to the reported uncertainty σ_i. We imposed Jeffreys priors, i.e., log-uniform distributions for all parameters except T, for which we imposed a Gaussian prior based on the period estimated from the sine+box function described earlier. We adopted the following likelihood function:

$$\log \mathcal{L} = -\frac{N}{2}\log 2\pi - \frac{1}{2}\log|\boldsymbol{C}| - \frac{1}{2}\boldsymbol{r}^{\rm T}\boldsymbol{C}^{-1}\boldsymbol{r}, \quad (5)$$

where N is the total number of measurements, $\boldsymbol{C}$ is the covariance matrix defined earlier, and $\boldsymbol{r}$ is the residual of the observed flux minus the box transit model.

We compared the Bayesian evidence of both models (GP and GP+box) using Dynesty, a nested sampling code (Speagle 2020). The Bayesian evidence was then used to compute the Bayes factor (for which ΔBIC is a proxy). We used the default settings on Dynesty. The sampling stopped automatically after standard convergence criteria were reached. We found that the GP+box model was favored by a Bayes factor of 3, which we interpret as only a marginal preference. The GP+box model (black line) is shown in Figure 9 (middle left panel). The box parameters for both the sine+box and GP+box fits are given in Table 2. Using the ratio of the depth parameter divided by its uncertainty as the S/N, the GP+box model gives a 4.2σ detection of an event.

As an aside, we noted during our MCMC analysis that the joint sine+box fit led to a somewhat different rotational period of the planet than the best-fit sine curve. Table 3 gives the best-fit planet variability parameters from this work (using the sine +box fit) and Schneider et al. (2018). We searched for a second periodic signal that might be attributed to the second IPMO but did not find any (see periodograms in Appendix B). Schneider et al. (2018) attempted to fit two sine curves to the data but were unable to identify a second rotation period. Further, we note that two IPMOs with similar rotation periods and amplitudes out of phase would not produce a sharp dip.

4.3. Possible Explanations for the Fading Event

In this section, we explore the possible explanations for the fading event. The most likely source of nonastrophysical systematic noise is the IRAC detector. To check on this possibility, we searched for (and did not find) any correlation between the extracted aperture flux and the centroid pixel coordinates on the Spitzer/IRAC detector. Nor did we find a significant displacement in the centroid position at the time of the fading event. The expected centroid shift due to a 1 hr, 1% flux change of one of the two unresolved IPMOs is $3\times$ smaller than the 1σ uncertainty in the centroid position measurement on this timescale.

An eclipse of one IPMO by the other IPMO, which is a priori very unlikely, is ruled out by the observed separation of 138 mas. The change in separation is only $\sim$2 mas yr^{-1}. What about the possibility of an unresolved eclipsing binary that is unrelated to the IPMOs? Best et al. (2017a) found only one background star that falls within the Spitzer aperture, at a separation of 3.″79. However, with a K-band magnitude that is 5.7 mag fainter than 2MASS J1119–1137AB, even a total eclipse of this background star would not lead to a decrease in relative flux by the observed amount.

The two most plausible explanations are (1) the dip is caused by the transit of a faint object such as a moon, disintegrating circumplanetary object, or another sort of transiently transiting debris (David et al. 2017), and (2) the dip is part of the erratic variability displayed by the IPMO due to clouds or other atmospheric features. We cannot distinguish between these possibilities with the available data. More helpful would be spectral observations of a fading event and confirmation of periodicity and consistency of the characteristics of the fading signals. This example highlights that the use of simultaneous multiband or spectral observations is needed for differentiating between exomoon transits and intrinsic IPMO variability. Because the exomoon explanation is interesting and the topic of this paper, we will explore it a bit further, keeping in mind that erratic variability is also a reasonable explanation.

To calculate the radius of the exomoon implied by the fractional loss of light requires an estimate for the radius of the IPMO, which is not given in the literature. We used the Fortney et al. (2007) exoplanet models to estimate the radius of the IPMO. Specifically, we used the models for the largest orbital distance in the library (9.5 au), figuring that this was the best match to a young planet for which the dominant heat source is internal rather than irradiation by the star. Assuming the objects have 25 $M_\oplus$ rocky cores and accounting for uncertainties in the age and mass of the system (as reported by Best et al. 2017a) leads to radius estimates of

$$R_A = R_B = 1.38^{+0.17}_{-0.11}\, R_{\rm Jup}. \quad (6)$$

This radius is also consistent with the evolutionary models of Saumon & Marley (2008). Under the assumption that the IPMOs are identical, we can calculate the moon's radius despite the fact that we do not know which IPMO is hosting the moon. We find $R_{\rm moon} = 1.74 \pm 0.19\, R_\oplus$ based on the fractional loss of light in the

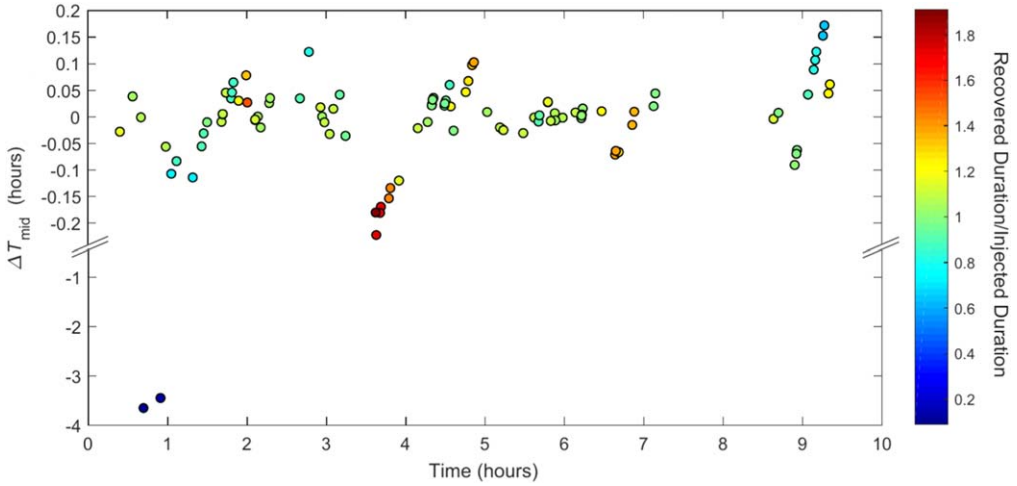

Figure 10. Results of an injection/recovery test. The error in the recovered value of the transit midpoint is shown as a function of the time at which the simulated transit was injected. The color of each point indicates the ratio of the recovered duration to the injected duration. In 98 out of 100 injections, the correct transit midpoint was recovered within 0.2 hr. In the other two cases, the sine fit was preferred over the sine+box fit, indicating no detection of an event.

GP+box model. A more detailed characterization, including a discussion of possible orbital parameters and the likelihood of habitability, is given in Appendix A.

To assess our sensitivity to transit signals in the data, we performed an injection/recovery test. We removed the real fading event from the data. We then injected 100 simulated transit events with the same duration and depth as the real dip, with parameters taken from the sine+box model. We did not inject any simulated transits within the portion of the data set covering the real fading event. We then fitted the simulated data with the sine and sine+box models using the same MCMC fitting method. We calculated the ΔBIC of the two models for all 100 cases, finding that the sine+box model was favored over the sine model 92% of the time. This indicates that a transit similar to the one detected can typically be recovered in this data set. Figure 10 shows the error in the recovered midpoint of the transit as a function of the time at which the signal was injected. In all but two of the injections, the recovered transit midpoint was within 12 minutes of the input value. This test illustrates that if a 40 minute transit by a $1.7\,R_{\oplus}$ moon had really occurred, we would probably have been able to detect it.

There are several possible approaches to follow up on this candidate signal. It may be possible to follow up with an 8 m class ground-based telescope in the *K* band. A single transit would be detectable at the $\approx 7\sigma$ level, and the IPMO variability cycle would be detectable after a full night of observations. Adaptive-optics imaging would allow the two components to be resolved; if a second transit were detected in spatially resolved observations, one could identify the host of the exomoon. However, the 2MASS J1119–1137AB variability has not been studied in the *K* band. If the IPMOs exhibit larger-amplitude or more erratic variability at this wavelength, or if the *K*-band instrumental systematics are larger than anticipated, transit detection will be hindered. Further, depending on the orbital period of the exomoon, many nights of observation could be required to catch a transit.

The JWST observations would be especially powerful. From Table 1, the JNSPP on this target is 66 ppm and would allow for a strong (50σ) detection of a similar fading event even if the IPMOs were unresolved. Spectrophotometric information would allow for the distinction between erratic IPMO variability (which is likely to be chromatic) and transits (for which the loss of light should not vary strongly with wavelength).

5. Summary

Based on analogies with the properties of the large moons of the giant planets in the solar system, the transits of moons around IPMOs are expected to be (1) common, occurring for 10%–15% of gas giant planets; (2) frequent, with orbital periods of a few days; and (3) possible to detect, with multiple moons per system that produce transit depths of 0.1%–2%. More than 50% or 33 of the 57 currently known IPMOs are sufficiently bright at near- and mid-infrared wavelengths to allow for $>5\sigma$ detection with JWST of single transits of Titan- or Ganymede-sized moons.

Bright young IPMOs are favorable targets because (1) they are typically larger in radius, increasing the geometric transit probability, and (2) the brightness allows for higher-precision photometry. The low masses and densities of IPMOs allow for the possibility of very close-orbiting moons with high transit probabilities. High transit probabilities are especially important because the transit search will need to be done on a target-by-target basis.

The search for exomoons transiting IPMOs will require substantial amounts of observing time on premier observatories. Will the community be willing to invest this much time? We note that thousands of hours of Spitzer and HST time were awarded to study IPMO and brown dwarf variability (e.g., the Weather on Other Worlds and Cloud Atlas programs; Metchev et al. 2015; Apai et al. 2017), independent of the motivation to search for transiting exomoons. Furthermore, JWST is scheduled to observe the IPMO WISE 0855 in Cycle 1 for 11 hr using the NIRSpec time-series G395M spectrum (Skemer et al. 2021). NIRspec will achieve a spectrally binned S/N of ≈4000 in 1 hr;[13] thus, the observation will be sensitive to exomoons as small as Titan/Ganymede with 5σ. Spectrally resolved time-domain models are needed that will allow us to discriminate between exomoon transit events and atmospheric variations/water-ice clouds in the WISE 0855 light curve.

[13] The S/N was calculated with a 250 K 1 $R_{\rm Jup}$ spectrum (Sonora 2018 grid; Marley et al. 2018) at 2.23 pc uploaded in JWST/ETC. Sensitivity is given in 1 hr and for the binned spectral sensitivity from $\lambda = 4$–5 μm ($R \approx 5$).

Development of such models can be done now so that we are prepared to search for exomoons in upcoming JWST IPMO data sets.

The moons of IPMOs might be some of the most observationally accessible habitable worlds. For young and hot IPMOs, JWST transmission spectroscopy of moons may be possible—and could be easier than it would be for a planet orbiting an M dwarf in some respects. Moons in the HZs of IPMOs transit every day or two, and in some cases, the transit depths may be as large as 2%. For older and cooler IPMOs, emission spectroscopy is potentially powerful, especially if the moon is tidally heated and comparable in temperature to its host. Further, these close-in exomoons are likely to lie in the IPMO's HZ (at least initially, until the planet cools), which will allow us to study conditions similar to primordial Earth and perhaps place limits on the timescale for the formation of life. If an HZ, 1.7 $R_\oplus$ exomoon exists around one of the components in 2MASS J1119–1137AB, JWST will be capable of securely detecting a single transit.

We are grateful to Darren L. DePoy for many useful discussions while preparing this manuscript. We thank an anonymous referee for a helpful and thorough review. M.A.L. acknowledges support from the George P. and Cynthia Woods Mitchell Institute for Fundamental Physics and Astronomy at Texas A&M University. JMV acknowledges support by NSF Award Number 1614527 and Spitzer Cycle 14 JPL Research Support Agreement 1627378. RH acknowledges support from the German Aerospace Agency (Deutsches Zentrum f\"ur Luft- und Raumfahrt) under PLATO Data Center grant 50OO1501.

This research has made use of the NASA Exoplanet Archive, which is operated by the California Institute of Technology, under contract with the National Aeronautics and Space Administration under the Exoplanet Exploration Program. This work has made use of the UltracoolSheet, maintained by Will Best, Trent Dupuy, Michael Liu, Rob Siverd, and Zhoujian Zhang and developed from compilations by Dupuy & Liu (2012), Dupuy & Kraus (2013), Liu et al. (2016), and Best et al. (2017b, 2020b).

Software: `emcee.py` (Foreman-Mackey et al. 2013), `astro.py` (https://github.com/astropy/astropy), `LombScargle` (VanderPlas 2017), `ELCA` (Pearson 2019), `Starry` (Luger et al. 2019), `corner.py` (Foreman-Mackey 2016), `numpy.py` (van der Walt et al. 2011), and `dynesty.py` (Speagle 2020).

Appendix A
The 2MASS J1119–1137AB Event Interpreted as an Exomoon Transit

If the event detected in the 2MASS J1119–1137AB Spitzer light curve is due to an exomoon transit, it is possible to constrain the exomoon orbital parameter space and characteristics based on the duration of the event. If we assume the event duration corresponds to the transit duration, we can determine the distance traveled, l, by the exomoon during the transit, assuming the IPMO is much more massive than the moon ($M_p \gg M_m$),

$$l = T_{\rm dur}\sqrt{\frac{GM_p}{a}}, \tag{A1}$$

where $T_{\rm dur}$ is the transit duration, M_p is the mass of the IPMO, and a is the exomoon's orbital distance. As explained earlier, the host IPMO's mass is either $M_1 \approx 3.7$ or $M_2 \approx 10\ M_{\rm Jup}$, depending on whether the system is part of the TW Hya association. To calculate the allowable parameter space for l, we consider both possibilities for M_p, use the measurement $T_{\rm dur} \approx 36$ minutes based on the GP fit, and allow a to be a free parameter. From l, we can calculate the impact parameter,

$$b = \sqrt{1 - \left(\frac{l - R_m}{2R_p}\right)^2}, \tag{A2}$$

where R_m is the radius of the moon. Using this equation for the impact parameter, we can calculate the allowable parameter space for the inclination, i, and orbital period, T, in the usual way (Winn 2010). Figure 11 gives the allowed inclination of the exomoon orbit as a function of a and T in the top left and right panels, respectively, for $M_p = M_1$ (black solid curve) and M_2 (red dashed curve). We can then calculate the equilibrium temperature of the exomoon with the equation

$$T_{\rm eq} = T_{\rm p,eff}(1 - \alpha_M)^{1/4}\sqrt{\frac{R_p}{2a}}, \tag{A3}$$

where α_M is the exomoon's albedo and $T_{p,\rm eff}$ is the planet's effective temperature. We assume $\alpha_M = 0.05$ (Heller & Barnes 2015) and $T_{p,\rm eff} = 1010$ K (Best et al. 2017a). The exomoon absorbs a time and spatially averaged flux

$$F = 239\ {\rm W\ m^{-2}}\ \frac{L_p(1 - \alpha_M)}{L_\odot(1 - \alpha_\oplus)}\left(\frac{1\ {\rm au}}{a}\right)^2, \tag{A4}$$

where $\alpha_\oplus = 0.3$. Using $L_p = 1.86 \times 10^{-5}\ L_\odot$ (Best et al. 2017a), we can calculate F. We assume that the HZ for the exomoon is defined by $83\ {\rm W\ m^{-2}} < F < 295\ {\rm W\ m^{-2}}$ (Kopparapu et al. 2013; Heller 2016). The bottom panels of Figure 11 show the calculated equilibrium temperature of the exomoon (from Equation (A3)) as a function of a and T. The shaded regions of these panels correspond to the HZ. Short-period orbits ($T \lesssim 5$ days) are more probable because (1) the transit probability of long-period orbits is low ($P < 8\%$ for $T > 5$ days) and (2) 20 hr of Spitzer observation covers <17% of the orbit for $T > 5$ days. Thus, if the exomoon is real, it is quite probable that it lies in the HZ. The Hill radius of either IPMO in this binary system is $R_{\rm H} = 1.3$ au. If the exomoon is orbiting with $T < 5$ days and $a < 0.009$ au (approximately the same orbital distance as Titan), then $a \ll R_{\rm H}$, and the exomoon would be dynamically stable.

Any inference about the exomoon's mass would depend on assumptions about its composition and on evolutionary models and are therefore highly uncertain. If the exomoon has a H/He envelope, it may be much less massive than might be inferred by comparison to older objects of similar radius. The current sample of detected exoplanets does not contain any planets smaller than $1.8\ R_\oplus$ and younger than 100 Myr. So, if the candidate signal corresponded to an exomoon, and further follow-up confirmed the moon, not only would it be the first confirmed exomoon, it would also be the youngest terrestrial-sized object, thereby offering a unique window into the properties of terrestrial worlds in their infancy.

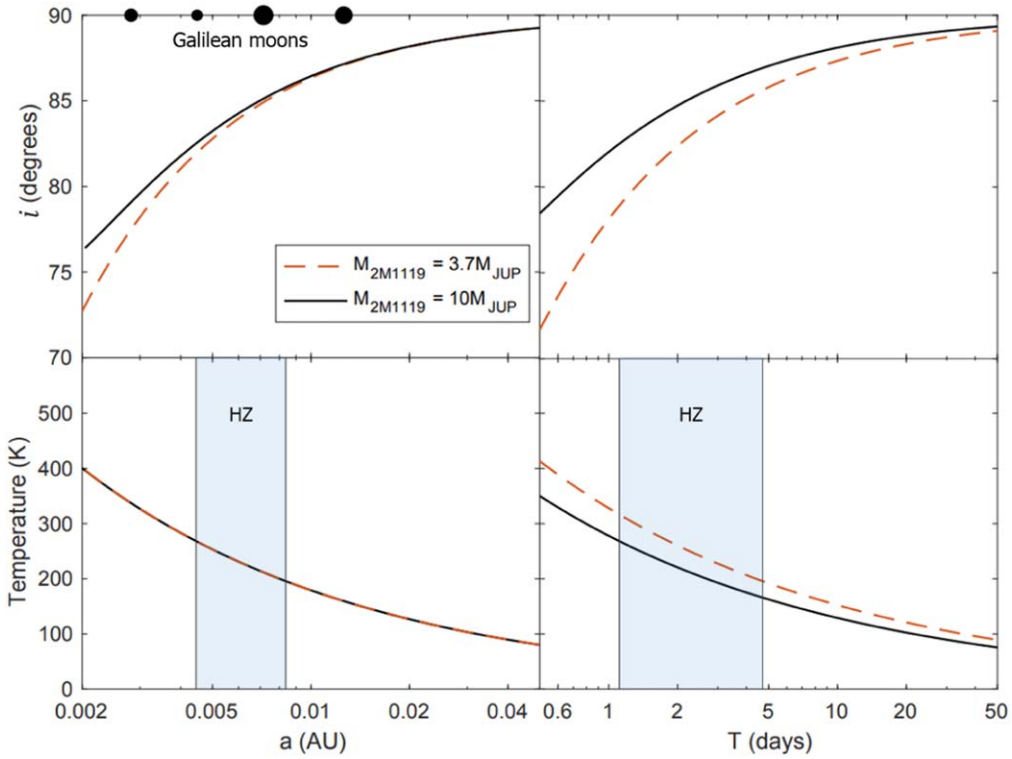

Figure 11. Top panels: allowed inclination of the exomoon's orbit as a function of orbital distance (left) and period (right) for the cases $M_p = 3.7$ (black solid curve) and 10 (red dashed curve) $M_{\rm Jup}$. The orbital distances of the four Galilean satellites are shown in the top left panel for reference. The lower limit on the period is 0.5 days based on the nonobservation of a second transit with Spitzer. Bottom panels: equilibrium temperature of the exomoon (from Equation (A3)) as a function of orbital distance (left) and period (right). The shaded regions correspond to the HZ.

Appendix B
Supplemental Figures from the Spitzer Light-curve Analysis

Figure 12 shows the Spitzer light curves of WISEA J1147-2040. Figure 13 is the corner plot from the sine+box MCMC fit. The periodograms from the 2MASS J1119-1137AB light curves are shown in Figure 14.

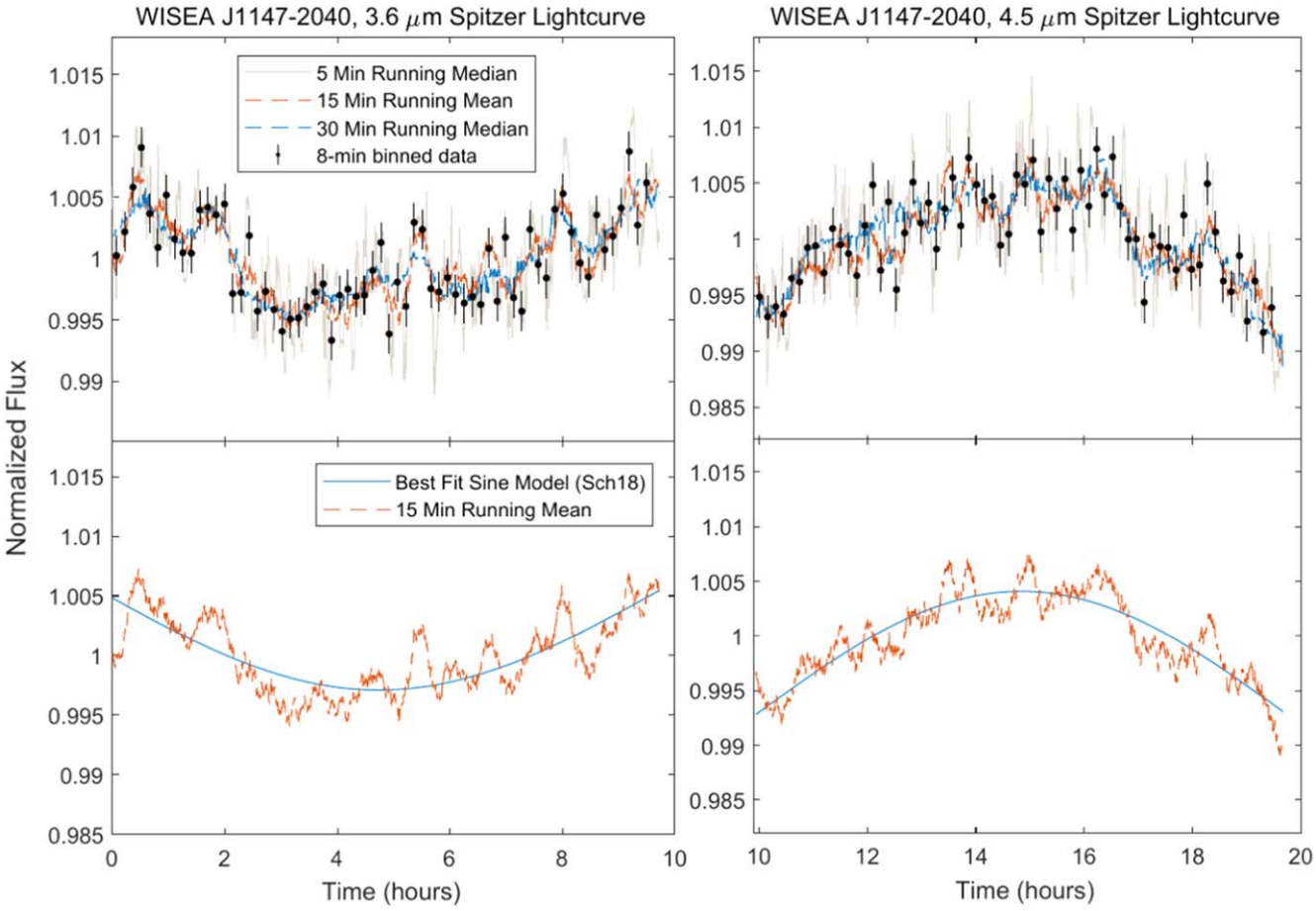

Figure 12. Top: Spitzer light curves of WISEA J1147–2040 based on a single 20 hr observation, 10 hr at 3.6 μm (left) and 10 hr at 4.5 μm (right). Bottom: in addition to the 15 minute running mean of the data (red dashed line) is the best-fit sine model (solid blue line) from the joint light-curve fit given in Schneider et al. (2018; since the rotation period is longer than the single-band observation, the joint fit is used in this case).

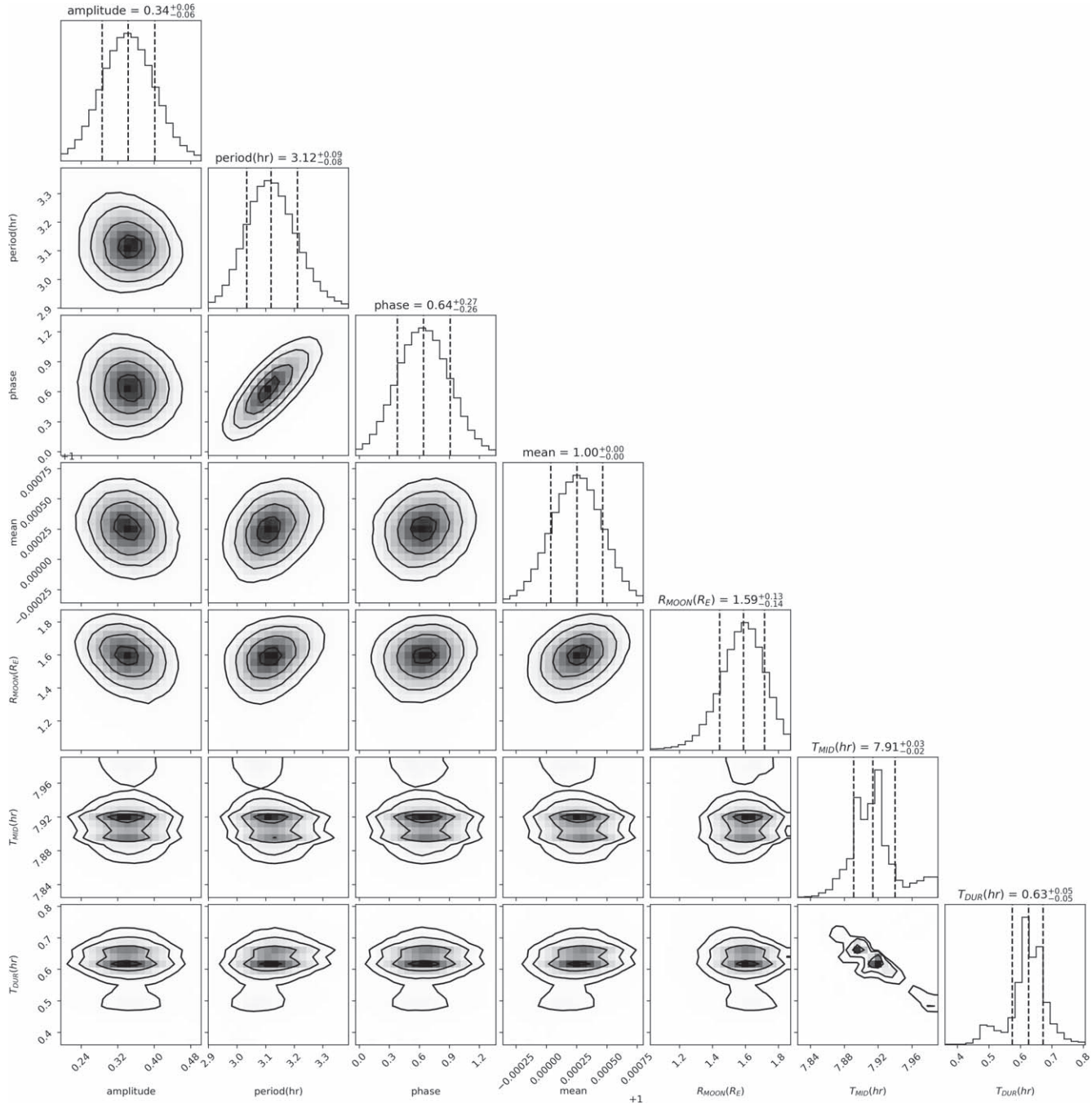

Figure 13. Corner plot from the sine+box MCMC fit of the Spitzer 3.6 μm 2MASS J1119–1137AB light curve.

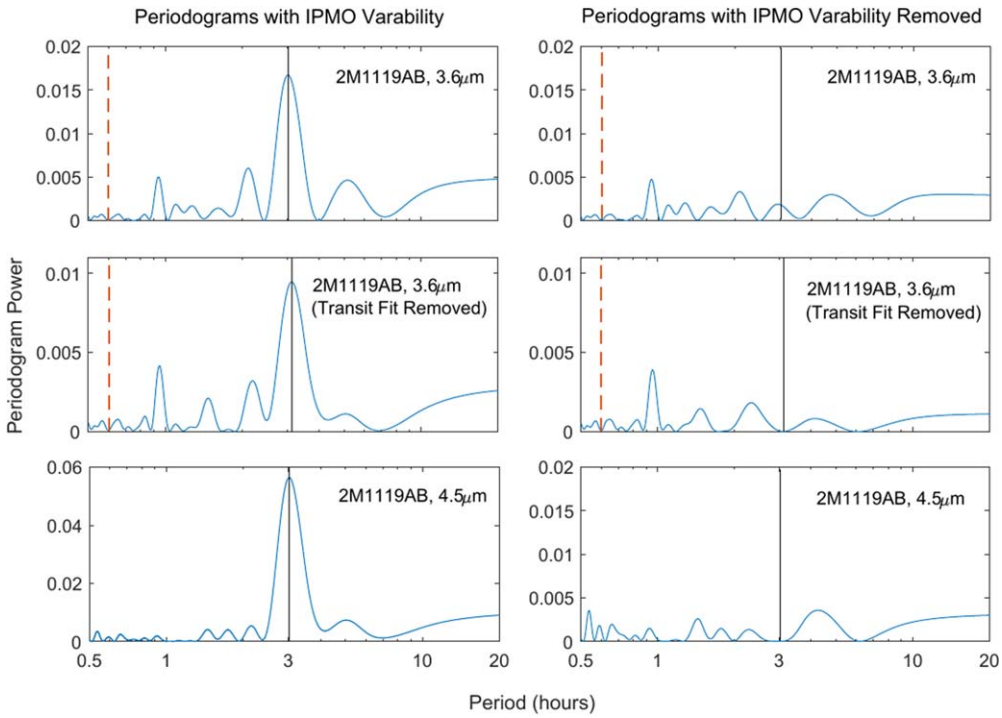

Figure 14. Periodograms of 2MASS J1119–1137AB. Left panels: periodograms including rotational variability. Right panels: periodograms with sinusoidal fit removed. The 3.6 μm Spitzer data periodograms are shown in the top two rows with the event included (top row) and removed (middle row). The 4.5 μm Spitzer data periodograms are in the bottom panels. The red dashed line is the duration of the event. The solid line is the best-fit rotational period of the IPMO.

ORCID iDs

Mary Anne Limbach https://orcid.org/0000-0002-9521-9798
Johanna M. Vos https://orcid.org/0000-0003-0489-1528
Joshua N. Winn https://orcid.org/0000-0002-4265-047X
René Heller https://orcid.org/0000-0002-9831-0984
Jeffrey C. Mason https://orcid.org/0000-0003-0035-598X
Adam C. Schneider https://orcid.org/0000-0002-6294-5937
Fei Dai https://orcid.org/0000-0002-8958-0683

References

Agol, E., Jansen, T., Lacy, B., Robinson, T. D., & Meadows, V. 2015, ApJ, 812, 5
Allers, K. N., Vos, J. M., Biller, B. A., & Williams, P. K. G. 2020, Sci, 368, 169
Apai, D., Karalidi, T., Marley, M. S., et al. 2017, Sci, 357, 683
Apai, D., Kasper, M., Skemer, A., et al. 2016, ApJ, 820, 40
Apai, D., Nardiello, D., & Bedin, L. R. 2021, ApJ, 906, 64
Apai, D., Radigan, J., Buenzli, E., et al. 2013, ApJ, 768, 121
Avila, P. J., Grassi, T., Bovino, S., et al. 2021, IJAsB, 20, 300
Baraffe, I., Homeier, D., Allard, F., & Chabrier, G. 2015, A&A, 577, A42
Bardalez Gagliuffi, D. C., Faherty, J. K., Schneider, A. C., et al. 2020, ApJ, 895, 145
Beatty, T. G., & Seager, S. 2010, ApJ, 712, 1433
Beaugé, C., & Nesvorný, D. 2012, ApJ, 763, 12
Benisty, M., Bae, J., Facchini, S., et al. 2021, ApJL, 916, L2
Ben-Jaffel, L., & Ballester, G. E. 2014, ApJL, 785, L30
Bennett, D. P., Batista, V., Bond, I. A., et al. 2014, ApJ, 785, 155
Best, W. M., Dupuy, T. J., Liu, M. C., Siverd, R. J., & Zhang, Z. 2020, The UltracoolSheet: Photometry, Astrometry, Spectroscopy, and Multiplicity for 3000+ Ultracool Dwarfs and Imaged Exoplanets v1.0.1, Zenodo, doi:10.5281/zenodo.4570814
Best, W. M. J., Liu, M. C., Dupuy, T. J., & Magnier, E. A. 2017a, ApJL, 843, L4
Best, W. M. J., Liu, M. C., Magnier, E. A., & Dupuy, T. J. 2020a, AJ, 159, 257
Best, W. M. J., Liu, M. C., Magnier, E. A., & Dupuy, T. J. 2020b, AJ, 161, 42
Best, W. M. J., Magnier, E. A., Liu, M. C., et al. 2017b, ApJS, 234, 1
Biller, B. A., Apai, D., Bonnefoy, M., et al. 2021, MNRAS, 503, 743
Biller, B. A., Vos, J., Buenzli, E., et al. 2018, AJ, 155, 95
Bowler, B. P. 2016, PASP, 128, 102001
Bowler, B. P., Zhou, Y., Morley, C. V., et al. 2020, ApJL, 893, L30
Buenzli, E., Apai, D., Radigan, J., Reid, I. N., & Flateau, D. 2014, ApJ, 782, 77
Burningham, B., Leggett, S. K., Homeier, D., et al. 2011, MNRAS, 414, 3590
Cabrera, J., & Schneider, J. 2007, A&A, 464, 1133
Canup, R. M., & Ward, W. R. 2002, AJ, 124, 3404
Canup, R. M., & Ward, W. R. 2006, Natur, 441, 834
Cilibrasi, M., Szulágyi, J., Grimm, S. L., & Mayer, L. 2021, MNRAS, 504, 5474
Cilibrasi, M., Szulágyi, J., Mayer, L., et al. 2018, MNRAS, 480, 4355
Cushing, M. C., Hardegree-Ullman, K. K., Trucks, J. L., et al. 2016, ApJ, 823, 152
Cushing, M. C., Kirkpatrick, J. D., Gelino, C. R., et al. 2011, ApJ, 743, 50
David, T. J., Petigura, E. A., Hillenbrand, L. A., et al. 2017, ApJ, 835, 168
de Mooij, E. J. W., & Snellen, I. A. G. 2008, A&A, 493, L35
Dupuy, T. J., & Kraus, A. L. 2013, Sci, 341, 1492
Dupuy, T. J., & Liu, M. C. 2012, ApJS, 201, 19
Dupuy, T. J., Liu, M. C., Allers, K. N., et al. 2018, AJ, 156, 57
Erkaev, N. V., Lammer, H., Elkins-Tanton, L. T., et al. 2014, P&SS, 98, 106
Esplin, T. L., Luhman, K. L., Cushing, M. C., et al. 2016, ApJ, 832, 58
Faherty, J. K., Rice, E. L., Cruz, K. L., Mamajek, E. E., & Núñez, A. 2013, AJ, 145, 2
Faherty, J. K., Riedel, A. R., Cruz, K. L., et al. 2016, ApJS, 225, 10
Filippazzo, J. C., Rice, E. L., Faherty, J., et al. 2015, ApJ, 810, 158
Foreman-Mackey, D. 2016, JOSS, 1, 24
Foreman-Mackey, D., Hogg, D. W., Lang, D., & Goodman, J. 2013, PASP, 125, 306
Fortney, J. J., Marley, M. S., & Barnes, J. W. 2007, ApJ, 659, 1661
Fox, C., & Wiegert, P. 2020, MNRAS, 501, 2378
Fulton, B. J., Petigura, E. A., Howard, A. W., et al. 2017, AJ, 154, 109
Gagné, J., Allers, K. N., Theissen, C. A., et al. 2018, ApJL, 854, L27
Gagné, J., Burgasser, A. J., Faherty, J. K., et al. 2015, ApJL, 808, L20
Gagné, J., Faherty, J. K., Burgasser, A. J., et al. 2017, ApJL, 841, L1
Ge, H., Zhang, X., Fletcher, L. N., et al. 2019, AJ, 157, 89
Gebek, A., & Oza, A. V. 2020, MNRAS, 497, 5271
Gelino, C., & Marley, M. 2000, in ASP Conf. Ser. 212, From Giant Planets to Cool Stars, ed. C. A. Griffith & M. S. Marley (San Francisco, CA: ASP), 322

Gelino, C. R., Kirkpatrick, J. D., & Burgasser, A. J. 2009, in AIP Conf. Ser. 1094, 15th Cambridge Workshop on Cool Stars, Stellar Systems, and the Sun, ed. E. Stempels (Melville, NY: AIP), 924
Gizis, J. E., Dettman, K. G., Burgasser, A. J., et al. 2015, ApJ, 813, 104
Goldman, B., Marsat, S., Henning, T., Clemens, C., & Greiner, J. 2010, MNRAS, 405, 1140
Gould, A., Pepper, J., & DePoy, D. L. 2003, ApJ, 594, 533
Hayashi, C., Nakazawa, K., & Mizuno, H. 1979, E&PSL, 43, 22
Heller, R. 2016, A&A, 588, A34
Heller, R. 2018, Handbook of Exoplanets (Berlin: Springer), 835
Heller, R., & Barnes, R. 2015, IJAsB, 14, 335
Heller, R., & Pudritz, R. 2015a, ApJ, 806, 181
Heller, R., & Pudritz, R. 2015b, A&A, 578, A19
Heller, R., Williams, D., Kipping, D., et al. 2014, AsBio, 14, 798
Hippke, M. 2015, ApJ, 806, 51
Hong, Y.-C., Raymond, S. N., Nicholson, P. D., & Lunine, J. I. 2018, ApJ, 852, 85
Inderbitzi, C., Szulágyi, J., Cilibrasi, M., & Mayer, L. 2020, MNRAS, 499, 1023
Kellogg, K., Metchev, S., Gagné, J., & Faherty, J. 2016, ApJL, 821, L15
Kenworthy, M. A., & Mamajek, E. E. 2015, ApJ, 800, 126
Kipping, D. 2020, ApJL, 900, L44
Kirkpatrick, J. D., Cushing, M. C., Gelino, C. R., et al. 2011, ApJS, 197, 19
Kirkpatrick, J. D., Gelino, C. R., Cushing, M. C., et al. 2012, ApJ, 753, 156
Kirkpatrick, J. D., Gelino, C. R., Faherty, J. K., et al. 2021, ApJS, 253, 7
Kopparapu, R. K., Ramirez, R., Kasting, J. F., et al. 2013, ApJ, 765, 131
Kraus, S., Le Bouquin, J.-B., Kreplin, A., et al. 2020, ApJL, 897, L8
Kreidberg, L., Luger, R., & Bedell, M. 2019, ApJL, 877, L15
Lagrange, A. M., Bonnefoy, M., Chauvin, G., et al. 2010, Sci, 329, 57
Lagrange, A. M., Gratadour, D., Chauvin, G., et al. 2009, A&A, 493, L21
Lazzoni, C., Zurlo, A., Desidera, S., et al. 2020, A&A, 641, A131
Leggett, S. K., Cushing, M. C., Hardegree-Ullman, K. K., et al. 2016, ApJ, 830, 141
Leggett, S. K., Tremblin, P., Esplin, T. L., Luhman, K. L., & Morley, C. V. 2017, ApJ, 842, 118
Lew, B. W. P., Apai, D., Zhou, Y., et al. 2020, AJ, 159, 125
Liu, M. C., Dupuy, T. J., & Allers, K. N. 2016, ApJ, 833, 96
Liu, M. C., Magnier, E. A., Deacon, N. R., et al. 2013, ApJL, 777, L20
Lopez, E. D., & Fortney, J. J. 2014, ApJ, 792, 1
Luger, R., Agol, E., Foreman-Mackey, D., et al. 2019, AJ, 157, 64
Luhman, K. L. 2014, ApJL, 786, L18
Luhman, K. L., Burgasser, A. J., & Bochanski, J. J. 2011, ApJL, 730, L9
Luhman, K. L., Burgasser, A. J., Labbé, I., et al. 2012, ApJ, 744, 135
Manjavacas, E., Apai, D., Lew, B. W. P., et al. 2019a, ApJL, 875, L15
Manjavacas, E., Apai, D., Zhou, Y., et al. 2019b, AJ, 157, 101
Marley, M., Saumon, D., Morley, C., & Fortney, J. 2018, Sonora 2018: Cloud-free, Solar Composition, Solar C/O Substellar Atmosphere Models and Spectra v1.0, Zenodo, doi:10.5281/zenodo.1309035
Mazeh, T., Holczer, T., & Faigler, S. 2016, A&A, 589, A75
Metchev, S. A., Heinze, A., Apai, D., et al. 2015, ApJ, 799, 154
Metchev, S. A., & Hillenbrand, L. A. 2006, ApJ, 651, 1166
Miguel, Y., & Ida, S. 2016, Icar, 266, 1
Misener, W., & Schlichting, H. E. 2021, MNRAS, 503, 5658
Miyazaki, S., Sumi, T., Bennett, D. P., et al. 2018, AJ, 156, 136
Mohanty, S., Jayawardhana, R., Huélamo, N., & Mamajek, E. 2007, ApJ, 657, 1064
Moraes, R. A., Kley, W., & Vieira Neto, E. 2018, MNRAS, 475, 1347
Mordasini, C., Alibert, Y., Georgy, C., et al. 2012, A&A, 547, A112
Mosqueira, I., & Estrada, P. R. 2003, Icar, 163, 198
Naud, M.-E., Artigau, É., Rowe, J. F., et al. 2017, AJ, 154, 138
Nutzman, P., & Charbonneau, D. 2008, PASP, 120, 317
Ogihara, M., & Ida, S. 2012, ApJ, 753, 60
Owen, J. E. 2020, MNRAS, 498, 5030
Owen, J. E., & Wu, Y. 2017, ApJ, 847, 29
Oza, A. V., Johnson, R. E., Lellouch, E., et al. 2019, ApJ, 885, 168
Parsons, S. G., Gänsicke, B. T., Marsh, T. R., et al. 2018, MNRAS, 481, 1083
Pearson, K. A. 2019, AJ, 158, 243
Rabago, I., & Steffen, J. H. 2018, MNRAS, 489, 2323
Radigan, J., Jayawardhana, R., Lafrenière, D., et al. 2012, ApJ, 750, 105
Radigan, J., Lafrenière, D., Jayawardhana, R., & Artigau, E. 2014, ApJ, 793, 75
Rappaport, S., Sanchis-Ojeda, R., Rogers, L. A., Levine, A., & Winn, J. N. 2013, ApJL, 773, L15
Reipurth, B., & Mikkola, S. 2015, AJ, 149, 145
Ricker, G. R., Winn, J. N., Vanderspek, R., et al. 2015, JATIS, 1, 014003
Roche, E. 1849, Académie des Sciences de Montpellier: Mémoires de la Section des Sciences, 1, 243
Rodenbeck, K., Heller, R., Hippke, M., & Gizon, L. 2018, A&A, 617, A49
Rogers, J. G., Gupta, A., Owen, J. E., & Schlichting, H. E. 2021, arXiv:2105.03443
Rogers, J. G., & Owen, J. E. 2021, MNRAS, 503, 1526
Rogers, L. A., Bodenheimer, P., Lissauer, J. J., & Seager, S. 2011, ApJ, 738, 59
Ronnet, T., & Johansen, A. 2020, A&A, 633, A93
Sada, P. V., Deming, D., Jackson, B., et al. 2010, ApJL, 720, L215
Sahoo, A., Guyon, O., Lozi, J., et al. 2020, AJ, 159, 250
Sanchis-Ojeda, R., Rappaport, S., Winn, J. N., et al. 2014, ApJ, 787, 47
Sasaki, T., Stewart, G. R., & Ida, S. 2010, ApJ, 714, 1052
Saumon, D., & Marley, M. S. 2008, ApJ, 689, 1327
Schneider, A. C., Cushing, M. C., Kirkpatrick, J. D., et al. 2014, AJ, 147, 34
Schneider, A. C., Cushing, M. C., Kirkpatrick, J. D., et al. 2015, ApJ, 804, 92
Schneider, A. C., Hardegree-Ullman, K. K., Cushing, M. C., Kirkpatrick, J. D., & Shkolnik, E. L. 2018, AJ, 155, 238
Schneider, A. C., Windsor, J., Cushing, M. C., Kirkpatrick, J. D., & Wright, E. L. 2016, ApJL, 822, L1
Scholz, R. D. 2010, A&A, 515, A92
Skemer, A., Miles, B. E., Morley, C., et al. 2021, JWST Proposal, 1
Skowron, J., Udalski, A., Szymański, M. K., et al. 2014, ApJ, 785, 156
Southworth, J. 2014, arXiv:1411.1219
Speagle, J. S. 2020, MNRAS, 493, 3132
Spiegel, D. S., Burrows, A., & Milsom, J. A. 2011, ApJ, 727, 57
Stökl, A., Dorfi, E., & Lammer, H. 2015, A&A, 576, A87
Stökl, A., Dorfi, E. A., Johnstone, C. P., & Lammer, H. 2016, ApJ, 825, 86
Tamburo, P., & Muirhead, P. S. 2019, PASP, 131, 114401
Tamburo, P., Muirhead, P. S., McCarthy, A., et al. 2021, in Cambridge Workshop on Cool Stars, Stellar Systems, and the Sun, 171, Zenodo doi:10.5281/zenodo.4565388
Tan, X., & Showman, A. P. 2021, MNRAS, 502, 2198
Teachey, A., Kipping, D., Burke, C. J., Angus, R., & Howard, A. W. 2020, AJ, 159, 142
Teachey, A., & Kipping, D. M. 2018, SciA, 4, eaav1784
Teachey, A., Kipping, D. M., & Schmitt, A. R. 2018, AJ, 155, 36
Triaud, A. H. M. J., Gillon, M., Selsis, F., et al. 2013, arXiv:1304.7248
van der Walt, S., Colbert, S. C., & Varoquaux, G. 2011, CSE, 13, 22
Van Eylen, V., Dai, F., Mathur, S., et al. 2018, MNRAS, 478, 4866
Vanderburg, A., Rappaport, S. A., & Mayo, A. W. 2018, AJ, 156, 184
VanderPlas, J. T. 2017, arXiv:1703.09824
Vos, J. M., Allers, K. N., & Biller, B. A. 2017, ApJ, 842, 78
Vos, J. M., Allers, K. N., Biller, B. A., et al. 2018, MNRAS, 474, 1041
Vos, J. M., Biller, B. A., Allers, K. N., et al. 2020, AJ, 160, 38
Vos, J. M., Biller, B. A., Bonavita, M., et al. 2019, MNRAS, 483, 480
Winn, J. N. 2010, in Exoplanet Transits and Occultations, ed. S. Seager (Tucson, AZ: Univ. Arizona Press), 55
Wright, J. T., Marcy, G. W., Howard, A. W., et al. 2012, ApJ, 753, 160
Zhang, Z., Liu, M. C., Best, W. M. J., Dupuy, T. J., & Siverd, R. J. 2021, ApJ, 911, 7
Zhang, Z., Liu, M. C., Claytor, Z. R., et al. 2021, ApJL, 916, L11
Zhou, G., Huang, C. X., Bakos, G. Á., et al. 2019, AJ, 158, 141
Zhou, Y., Apai, D., Schneider, G. H., Marley, M. S., & Showman, A. P. 2016, ApJ, 818, 176
Zhou, Y., Bowler, B. P., Morley, C. V., et al. 2020, AJ, 160, 77